Stability Analysis and Performance Optimization for the Multi-Parallel Grid inverters System

Lu, Minghui

Publication date:
2017

Document Version
Version created as part of publication process; publisher's layout; not normally made publicly available

STABILITY ANALYSIS AND PERFORMANCE OPTIMIZATION FOR THE MULTI-PARALLEL GRID INVERTERS SYSTEM

by

Minghui Lu

AALBORG UNIVERSITY
DENMARK

Dissertation submitted

.

Thesis submitted: June 14, 2017

PhD supervisor: Prof. Frede Blaabjerg,
Aalborg University

Assistant PhD supervisor: Associate Prof. Xiongfei Wang,
Aalborg University

PhD committee:

Prof. Weihao Hu (chairman),
Aalborg University

Prof. Robert S. Balog,
Texas A&M University

Prof. Maryam Saeedifard,
Georgia Institute of Technology

PhD Series: Faculty of Engineering and Science, Aalborg University

ISSN: xxxx- xxxx
ISBN: xxx-xx-xxxx-xxx-x

Published by:
Aalborg University Press
Skjernvej 4A, 2nd floor
DK – 9220 Aalborg Ø
Phone: +45 99407140
aauf@forlag.aau.dk
forlag.aau.dk

Printed in Denmark by Rosendahls, 2017

CV

Minghui Lu was born in China. He received the B.S. degree from Harbin Institute of Technology, Harbin, China in 2011, and the M.S. degree from Huazhong University of Science and Technology, Wuhan, China in 2014, both in electrical engineering. He is currently working toward the Ph.D. degree at the Department of Energy Technology, Aalborg University, Aalborg, Denmark. His research interests include power converters and their grid applications, control and stability analysis of power electronic based power systems. Minghui Lu is a Student Member of the Institute of Electrical and Electronics Engineers (IEEE), the IEEE Power Electronics Society, and the IEEE Industry Applications Society. He serves as a reviewer for several top journals and conferences, such as IEEE Transactions on Industrial Informatics (TII), IEEE Transactions on Industrial Electronics (TIE) and IEEE Journal of Emerging and Selected Topics in Power Electronics (JESTPE), IEEE ECCE, APEC, EPE conferences.

ENGLISH SUMMARY

With the development of highly penetrated renewable energy generation systems, power electronics converters have been widely employed in the modern power system. Although these power converters are able to realize efficient power conversion between renewables and the grid, they bring the resonance and instability problems at the same time. Hence, many advanced schemes have been developed to attenuate the undesirable resonances and to avoid the system instability. However, it is still a challenge for the manufacturers and research institutes to maintain high performance of power converters in the complex grid conditions, for instance the power grid is weak or contains background voltage harmonics.

Fortunately, thanks to the development of the power semiconductor devices and more advanced digital microprocessors, many innovative control strategies and system optimization design guidelines are proposed, which will promote the product development of future power converters. In this context, this thesis presents several technical chapters on the stability analysis and performance optimization of grid-connected voltage source inverters with LCL-filter. Firstly, in order to mitigate the influence of grid voltage background harmonics, Grid Voltage Feedforward Regulator (GVFR) is commonly adopted in the grid-connected applications. This thesis analyzes the impacts of the GVFR on system stability when the power grid is weak. Meanwhile, a robust design guideline for the LCL-filter is proposed to adapt the inverters to the weak grid condition. On the other hand, to optimize the output performance and dynamics of the grid-connected inverters using digital microprocessor as the controller, the digital time delays need to be compensated. The origin of these digital delays is clearly revealed in the thesis, moreover, the basic principle for existing time delay compensation schemes are explained using a unified graphical evaluation method. Besides, an improved delay compensation scheme is proposed based on the comparison of various compensation schemes in this thesis.

Finally, the parallel operation of multiple parallel grid-connected inverters has been addressed. It has been reported that the interactions between these parallel inverters may excite resonance in the distributed power system. This thesis has developed a current separation model to analyze the system stability using two separate stability criterion. Apart from the resonant current injected into the power grid, the current circulating between these parallel inverters also may excite the resonance.

All the theoretical analysis in this thesis have been verified by simulation or/and experimental results. These contributions have been published/submitted through 3 journal papers and 7 conference papers.

DANSK RESUME

Med udviklingen af stærkt penetrerede vedvarende energiproduktionssystemer har kraftelektronik-omformere været brugt i det moderne el system. Selvom disse kraftomformere er i stand til at realisere effektiv strømkonvertering mellem vedvarende energikilder og nettet, bringer de resonans- og ustabilitetsproblemerne på samme tid. Derfor er mange avancerede ordninger blevet udviklet til at dæmpe de uønskede resonanser og for at undgå systemets ustabilitet. Det er dog stadig en udfordring for fabrikanterne og forskningsinstitutterne at opretholde højkonverteringsomformere i de komplekse net forhold, for eksempel strømnettet er svagt eller indeholder baggrundsspændingsovertoner.

Heldigvis er mange innovative styringsstrategier og system optimerings design retningslinjer, takket være udviklingen af krafthalvlederindretningerne og mere avancerede digitale mikroprocessorer, foreslået, som vil fremme produktudviklingen af fremtidens effektomformere. I denne sammenhæng præsenterer denne afhandling flere tekniske kapitler om stabilitetsanalyse og ydeevneoptimering af net forbundne spændingskildeomformere med LCL-filter. For det første for at mindske indflydelsen af net spændingens baggrundsmønstre, er net spændingsforsynings regulator (GVFR) almindeligt vedtaget i de net forbundne applikationer. Denne afhandling analyserer GVFR's indvirkning på systemstabilitet, når strømnettet er svagt. I mellemtiden foreslås en robust designretningslinje for LCL-filteret til at tilpasse omformerne til den svage gittertilstand. På den anden side skal de digitale tidsforsinkelser kompenseres for at optimere udgangseffektiviteten og dynamikken hos de net forbundne omformere ved hjælp af digitale mikroprocessor som regulator. Oprindelsen af disse digitale forsinkelser afsløres tydeligt i afhandlingen. Desuden forklares grundprincippet for eksisterende tidsforsinkelsesordninger ved hjælp af en samlet grafisk evalueringsmetode. Desuden foreslås en forbedret forsinkelseskompensationsordning baseret på sammenligning af forskellige kompensationsordninger i denne afhandling.

Endelig er paralleloperationen af flere parallelle net forbundne omformere blevet adresseret. Det er blevet rapporteret, at samspillet mellem disse parallelle invertere kan vække resonans i det distribuerede el system. Denne afhandling har udviklet en nuværende separationsmodel til analyse af systemstabilitet ved anvendelse af to separate stabilitetskriterier. Bortset fra resonansstrømmen injiceret i el nettet, kan strømmen, der cirkulerer mellem disse parallelomformere, også ophidses resonansen.

Den teoretiske analyse i denne afhandling er blevet verificeret ved simulering eller / og eksperimentelle resultater. Disse bidrag er blevet offentliggjort / indsendt via 3 journalartikler og 7 konferenceartikler.

ACKNOWLEDGEMENTS

I really appreciate the financial support from the China Scholarship Council (CSC) and Harmony Project under European Research Council (ERC) during my Ph.D. period. I would like to express my sincere thanks to Department of Energy Technology, Aalborg University, Otto Mønsteds Fund and Mr. Yun Zhang from Embassy of The P.R. China in the Kingdom of Denmark.

It is a genuine pleasure to express my deep sense of thanks and gratitude to my supervisor Prof. Frede Blaabjerg for his patient guidance, constant encouragement and meticulous scrutiny. He provides us active academic environment and efficient platform for research. His dedication and sincere attitude to help his students impresses me a lot. Without his supervision and help, I could not finish my Ph.D. study.

I owe a deep sense of gratitude to my co-supervisors, Professor Xiongfei Wang and Professor Poh Chiang Loh, who play an important role during my research life in Aalborg. I benefit a lot from their instructive advices, prompt inspirations and interactive discussion. It is them who taught me how to do research. Many thanks to other *Harmony Project* members, they are Prof. Claus Leth Bak, Dr. Yi Tang, Haofeng Bai, Jun bum Kwon, Changwoo Yoon, Esmaeil Ebrahimzadeh. Thank you for fruitful discussion and sharing.

I want to thank profusely Professor Huai Wang and Professor Yongheng Yang for their care and suggestions in the life. Their help with kindness brings me convenience, making me focusing on my work. I am extremely thankful to my friend Dr. Zhen Xin for giving me necessary suggestions during the whole Ph.D. study. Pure friendship with him makes the Ph.D. period full of fun.

I would like to take this opportunity to thank the assessment committee for my Ph.D. defence, they are Prof. Weihao Hu, Prof. Robert S. Balog from Texas A&M University and Prof. Maryam Saeedifard from Georgia Institute of Technology and Prof. Francesco Iannuzzo. Thank all of you for sparing a time to evaluate my thesis and attend my defence.

Many thanks go to my colleagues in the Department of Energy Technology, Aalborg University, they are Zi'an Qin, Dao Zhou, Dongsheng Yang, Yanbo Wang, Dapeng Lu, Bo Sun, Qian Wu, Qian Wang, Dan Wu, Min Huang, Yanfeng Shen, Haoran Wang, Qing Zeng, Baoze Wei, Rui Hu, Dong Liu, Chi Zhang, Tomislav Dragicevic, Zhan Shen, Yi Zhang. Moreover, many appreciations are given to Tina Larsen, Hanne Munk Madsen.

I also would like to thank the guest professors and students in Aalborg University, it is a wonderful experience to make friends with all of you, they are Dr. Shaowei Qing, Dr. Yang Liu, Dr. Wen Wang, Dr. Qingsong Wang, Dr. Ronggang Ni, Haijin Li, Dr. Xiong Xiong, Zhen Zhang, Dr. Hao Yi, Dr. Qi Zhang, Dr. Gan Zhang, Dr. Gang Zhang.

Many thanks to the professors and friends during exchange in the Petroleum Institute, they are Professor S.M. Muyeen, Professor Ahmed Al Durra, Dr. Siyu Leng, Yunfei Guo, Jiayi Wang, thank fate let us meet.

I am extremely thankful to my parents and sister for their everlasting love, concerns and support. With their love, I am of more braveness to face and conquer the difficulties throughout my life.

Minghui Lu

May 11, 2017
Pontoppidanstræde 101, Room 47
Aalborg University, Denmark

TABLE OF CONTENTS

TABLE OF FIGURES

LIST OF TABLES

CHAPTER 1. INTRODUCTION

This *Introduction* chapter firstly presents the background and motivation of this Ph.D. thesis. Then, a short state-of-the art of the technical parts in this thesis is presented. Meanwhile, the research objectives and limitation are also given. Finally, the thesis structure and outline are shown to give a clear picture about the sequence of this research work. All the publications submitted during the Ph.D. period are listed at the end of this chapter.

1.1. BACKGROUND AND MOTIVATION

In the past few decades, the energy structure in many European countries (e.g. Denmark, Netherlands and Germany) has experienced a major transition from fossil-fuels based resources to green and clean renewables [1], [2]. By the end of 2016, the global cumulative installed wind energy capacity reached at least 486 GW according to the statistics released by Global Wind Energy Council [3]. With the similar trend, global cumulative installed PhotoVoltaic (PV) capacity exceeds 302 GW [4]. The overall renewables supply more than 4.7% of global electricity demands [4]. Especially, it is expected that, in Denmark, 100% electricity demands are supplied by renewables in 2050 [2]. It can be predicted that the penetration rate of renewables is going to be further increased in the near future.

In this context, in order to realize the efficient energy conversion between these natural-resources based renewables and the power grid, an increasing number of grid-connected power converters are installed in the modern power system [5]. These converters act as the role of interfaces to supply higher quality electricity to the power grid, assuring the renewable energy ready for grid integration. This situation makes the modern power system more and more power-electronics based [6]. However, it has been gradually revealed that highly-penetrated power electronics converters in the power system may lead to potential problems in terms of safe operation and power quality issues [7]-[14], which are attracting increasing research attention recently.

Figure 1-1 shows the circuit topology and control system of a typical grid-connected voltage source inverter with LCL-filter. The Pulse Width Modulation (PWM) technique is adopted to control the semiconductor switches [15]. In order to filter out the high-frequency harmonics from the switching process, an output power filter is required to meet the grid standards (e.g. IEEE 1547-2003 [16]). Among various filter options, the LCL-filter is widely used in the practical application due to its strong filtering ability with even reduced reactive element volume and cost [17]-[20]. For the control system, generally, the classical cascade control loops are employed to regulate the voltage or current to guarantee a satisfactory power quality. As shown in Figure 1-1, the outer loop includes Phase Locked Loop (PLL) [21], DC-

link voltage control [22], [23], Maximum Power Point Tracking (MPPT), power control while the inner loop contains current control [24], damping scheme [25], harmonic control [26] and feedforward control [27]. The outer loop and inner loop are designed to decouple with each other to make system controllable.

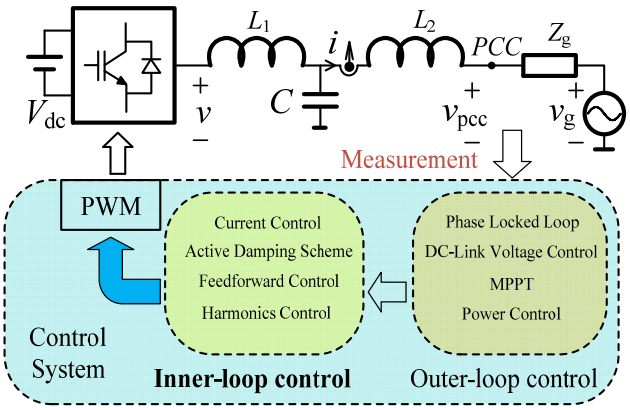

Figure 1-1 Topology and control structure of a grid-connected inverter with LCL filter [39].

For the above-mentioned configuration of grid-connected inverters, many issues in terms of stable operation, control performance, especially in uncertain grid condition, need more investigation. In this thesis, three selected research topics are discussed and studied as follows

(*a*) How to maintain high performance of power inverters in weak power system: The robustness against the grid impedance variation is of much significance for grid-connected inverters. This thesis deals with a robust design guideline for LCL-filter of inverter considering the Grid Voltage Feedforward Regulator (GVFR) to adapt to the uncertain grid condition. Meanwhile, the impacts of the GVFR on LCL-filtered system stability are also identified.

(*b*) How to improve the control performance of power inverters with digital controller: Digital processors, e.g. DSP and FPGA, are commonly used in the control systems of grid-connected inverters to flexibly execute control algorithm and modulation process [33]. Such a system will bring digital time delays into the control loop, which may lead to a reduced control loop bandwidth and even unstable dynamics [34]. It is also an interesting topic to discuss how to effectively compensate these delays to improve control performance.

(*c*) Discuss the impacts of increasingly high-penetrated renewables on system stability: To scale up the total capacity of renewables generation, dozens or even hundreds of grid-connected inverters operate in parallel [10], [20]. The interactions

and couplings among these inverter modules tend to aggravate the system oscillations and instability problems [8].

1.2. STATE OF THE ART

1.2.1. HARMONICS AND RESONANCE IN A INVERTER SYSTEM

a) Switching harmonics: Generally, most modern power-electronics inverters use fully controllable switching devices, e.g. Insulated Gate Bipolar Transistors (IGBT) and Metal-Oxide-Semiconductor Field-Effect Transistors (MOSFET), to build the converter bridge topology [35]. With the PWM technique employed, switching frequency harmonics are hereby produced in the inverter output voltage and propagate in the system. The frequency of harmonics ranges from several kHz to several hundreds of kHz. Typically, power filters are required to eliminate these harmonics, such as series inductor L-filter and high-order LCL-filter.

b) Harmonics caused by reactive components: Resonance caused by reactive elements, e.g. inductor and capacitor, may challenge the safe operation of the power system [7]. The inductance and capacitance in power filters (e.g. LCL-filter) and reactive power compensation units as well as the parasitic elements in the transmission cables may introduce complex system resonances into the power system [36]. Moreover, the output filters might interact with other passive components in the power distribution system, which may cause additional resonance hazard in the system [36].

c) Instability and harmonics caused by digital time delays: In the ac conversion system, the current control loop plays a critical role in regulating the injected power quality [34]. A direct method to control the current is to adopt a simple linear Proportional-Integral (PI) or Proportional-Resonant (PR) regulator [37]. Such a system has no theoretical stability limits because the phase plot never crosses the -180°. However, digital delays, which inevitably exist in a digitally-controlled system, will decrease the system phase margin, resulting in a limited control gain [38]. The instability undesirably arises if the control gain exceeds the limit value.

1.2.2. GRID-VOLTAGE FEEDFORWARD SCHEME

In a grid-connected system, the grid voltage background harmonics, which acts as the disturbance in the control loop, may pollute the output grid current. In order to suppress the current distortion, two different approaches are widely adopted: 1) Traditional current controller with selective harmonics compensation, in which multiple PR controllers are required [26], [40]; 2) An alternative is the grid-voltage feedforward scheme [27]-[32]. In comparison with the first solution, the Grid Voltage Feedforward Regulator (GVFR) has the advantages of simplicity, less computational burden.

In fact, the cause of the current distortion by the grid voltage harmonics is that the output admittance provides a path for the harmonics. In [28], a harmonic impedance concept is proposed to discuss the issues of the output current distortion. A so-called "full-feedforward" scheme of grid voltage is proposed in [27] and [29] to fully eliminate the high frequency current ripple caused by the grid background voltage harmonics. However, a second order derivative element is required, which is quite sensitive to the noises, making it difficult to implement such a scheme in a practical grid voltage feedforward application [42]. Besides the full-feedforward option, a traditional solution with unity feedforward gain is still widely used in grid-tied application [30]-[32], [39]. A co-design procedure for the LCL-filtered inverter considering the traditional grid voltage feedforward control is presented in [30]. A sampling instant shifting method is adopted to reduce delay in the grid voltage feedforward path [31]. [32] studies the stability of grid-parallel inverter with various grid impedance, demonstrating that the feedforward term would introduce the grid current positive feedback, degrading the system performance. The passive model of the feedforward control in a LCL-filtered inverter is derived in [39]. To compensate the delays in the voltage feedforward path, a repetitive predictor is adopted in [43]. In a weak power system, it have been reported that the GVFR will have significant impacts on the inverter stability [32], [38]. The influence of GVFR on LCL-filtered system needs more research attention.

1.2.3. DIGITAL TIME DELAY COMPENSATION METHODS

To compensate the digital delays in the digital controller [44], numerous techniques to compensate the delays are proposed [24], [44]-[54]. Generally, they can be divided into two main categories: a) model-free schemes and b) model-based schemes [46]. Their compensation performances are compared in detail in [55]. The implement of former is independent of the system modeling information while the latter is quite sensitive to system modeling accuracy. An inaccurate model cannot guarantee the effectiveness of the model-based methods. Therefore, in order to avoid the dependency, many model-free methods are developed [46].

In [44], a linear predictor concept is proposed based on the linear extrapolation theory [46]. It predicts the future data through the data in the past step. Its prediction ability has been demonstrated through an increased system bandwidth. However, it cannot guarantee satisfactory compensation effect at the high frequencies because a compulsive requirement $\omega \cdot T_d < 0.05$ is expected for the accurate linear extrapolation [44], [46]. Apart from the linear predictor, some compensation approaches based on the digital-filter structure have been developed in recent publications [24], [47], [49]. A First-Order-Filter (FOF) based compensator is adopted in [49], whose essence, in fact, is an Infinite Impulse Response (IIR) filter, which is configured in a feedback structure [46]. Compared to the linear predictor, this method can provide more effective and accurate delay compensation through a simple digital filter. However, it has the disadvantage of amplifying the noises at the frequencies near the

Nyquist frequency, where it has an infinite magnitude [46]. In [47], a modified FOF based compensation scheme is presented, in which two additional coefficients are introduced. Through changing the coefficient values, a tradeoff between the compensation ability and the noise attenuation can be obtained [46]. Besides the FOF based method, a so-called Second-Order Generalized-Integrator (SOGI) based compensator is adopted in [24] to reduce the delay in a grid converter. In fact, the essential idea is to take advantage of the phase-lead feature of the SOGI around the resonant frequency. Compared to FOF based scheme, its basic structure after discretization is a second-order digital IIR filter. For these mentioned compensation schemes, a unified evaluation method to compare their compensation ability and performance is therefore expected. This thesis will propose such an evaluation method in Chapter 3.

1.2.4. STABILITY ASSESSMENT FOR MULTIPLE PARALLELED GRID-CONNECTED INVERTERS

In modern power system, highly penetrated renewables usually adopt the LC-filtered or LCL-filtered grid-connected converters to transfer the natural energy to the power grid [56], [57]. And these converters usually operate in parallel. According to recent publications on this topic [7]-[14], [58], [59], the parallel operation of these converters would arouse the parallel capacitance-inductance resonance and its propagation in the distributed networks, which threat the safe operation of whole system. In this context, the system resonance can be divided into two levels as presented in Figure 1-2:

- *Individual grid-connected inverter self-resonance*, namely the harmonic resonance excited by every single grid-connected inverter module. The potential causes include the high order output filter resonance network [57] and the digital delay issues [39].
- *Multi-inverters interactive resonance*, namely the resonance between these parallel inverters and the grid impedance [8], [12], [13]. According to [8], these paralleled inverters are coupled to each other. The coupling and interactions among these converters would excite resonance and stability issues [20].

The problems above may limit the further development of the large-scale renewable power plant and impede the application of multiple grid-connected converters in parallel [12], [13], [20]. These questions push forward the research work on parallel operation of multiple grid-connected converters [20]. [7] reveals the resonance problem in a residential solar system, where many commercial power inverters are tied to the same point. A passive model without the controller is given to study the harmonics [20]. It has been demonstrated in [8] that the equivalent grid impedance is enlarged by N times if N identical converters are tied at the Point of Common Coupling (PCC) [20]. This analysis based on multi-variable theory [60] reveals the

reason why multiple inverters have different performance from the single inverter [13].

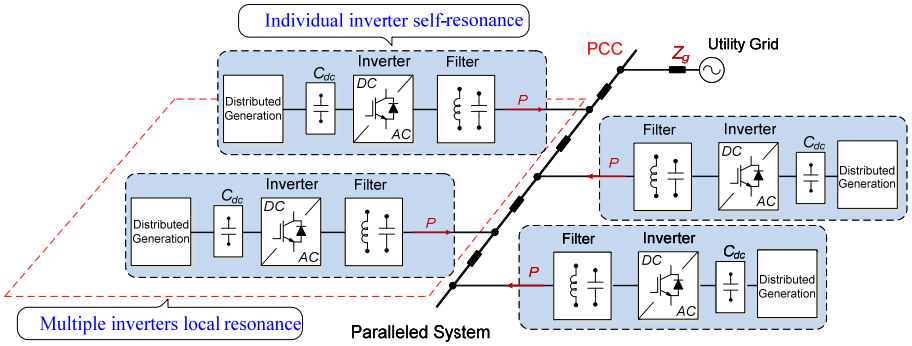

Figure 1-2 Parallel operation of multiple grid-connected converters.

[10] continues to analyze resonant characteristics in a inverters-based Microgrid, in which the module is modeled as Norton equivalent circuit [13]. Moreover, a virtual-impedance-based damping scheme is presented to stabilize the system. Similar modeling and analysis method is adopted in [59] to study the dynamic interactions in a two Active Power Filters (APFs) application [12]. [8] then proposes an external active damper for stabilizing multiple grid-connected inverters. [61] observes the circulating resonant current at filter resonance frequency in experiment results with two inverters, which operate under asynchronous carriers conditions. [62] discusses the interaction of grid-connected inverters when a large number of identically rated inverter modules are installed in parallel and deals with the grid voltage influence on the multiple inverters.

1.3. PROJECT OBJECTIVES AND LIMITATIONS

1.3.1. RESEARCH QUESTIONS AND OBJECTIVES

Many advanced schemes have been developed to attenuate the undesirable resonances and to avoid the system instability. However, it is still a challenge for the manufacturers and research institutes to maintain high performance of power converters in the complex grid conditions, for instance the power grid is weak or contains background voltage harmonics. Aiming at the aforementioned three research topics, this thesis further investigates the possible challenges and stability problems in the multi-parallel inverters system and sketches the corresponding objectives:

- *For the previous research on the stability analysis of LCL-filtered inverter, the Grid-voltage feedforward regulator is usually neglected. How does the GVFR affect the stability of grid-tied inverters with LCL-filter in the weak power*

system? Positive impact of stabilizing the system or negative impact of destabilizing the system?

The research objective is to systematically explore the stability of the LCL-filtered grid-connected inverter with grid-voltage feedforward regulator. Apart from the critical frequency concept, two more resonance frequency boundaries are derived using the Jury's criterion. Meanwhile, to adapt the grid-connected inverters to the weak power system, a robust design guideline for LCL-filter is studied.

- *What is the reason for the digital delays in a digitally-controlled system? To compensate these digital delays, numerous model-free delay compensation methods are developed. How to evaluate and compare these compensation methods through a unified approach? Is it possible to improve these existing compensation methods?*

This thesis tries to explain the compensation principle of existing methods using a graphical evaluation method. For each method, the impulse area concept can be introduced to illustrate the compensation ability. Based on the graphical evaluation, an improved compensation method with better performance is proposed.

- *What influences will be brought to the safe operation of the grid-connected converters by the increasing penetration of the renewables in the modern power system? In the highly-penetrated renewable energy system, how these interconnected inverters interact with each other?*

The research objective is to reveal the interactions and coupling of the multiple paralleled inverters in the renewables plant. The difference between single inverter case and multiple inverters should be presented. The reason why the couplings exist in the multiple inverters in the weak grid should be revealed.

1.3.2. RESEARCH LIMITATIONS

This thesis has focused on the stability analysis of the current control loop in the grid-connected inverters. The outer loops are assumed to be decoupled with inner current loop. The influence of outer loops, e.g. the PLL, the DC-link voltage control and power control loop are not considered in detail. Moreover, the modulation process is supposed always to operate within the linear area limited by the DC-link voltage [63]. The nonlinear impacts are out of scope of this thesis and will not be discussed here. Furthermore, all the verifying experiments in this thesis were done on the platform with the several kilowatts commercial inverters. However, this is not a full-picture representation for renewables only when a robust DC-link voltage control is guaranteed.

1.4. THESIS OUTLINE

This Ph.D. thesis is documented as ***a collection of articles***, including a summary report and a collection of the published papers. In the report, research work is briefly summarized through three main contributions. In the selected publications, relevant papers published during the Ph.D. period are attached selectively. The report contains 5 chapters and it is organized as follows:

Chapter 1 introduces the Ph.D. project background and motivation, state of the art, objective and list of publications.

Chapter 2 deals with the stability analysis and robust design of the grid-connected inverter with LCL-filter considering the grid-voltage feedforward regulator. The chapter starts with the stability analysis of current loop through system poles distribution identification. And the critical frequency and control gain limitation are hereby derived. And then the analysis extends to the case that the GVFR is adopted. Two resonance frequency boundaries are identified. Then, a robust design of LCL-filter for more adaptability to the complex grid condition is recommended.

Chapter 3 addresses the digital time delays compensation methods in a digitally-controlled converter. The compensation performances of these methods are evaluated and compared through a proposed graphical approach [46]. The impulse area is plotted and shown to illustrate the compensation effects of different methods. Then, an improved delay compensation method is proposed based on the same evaluation [46].

Chapter 4 focuses on the stability analysis of multiple paralleled inverters system. The chapter first presents the modeling of the interactive current and common current. The paralleled inverters are coupled to each other in the weak power system. It is revealed that the grid impedance makes the two currents have different stability ranges. Three cases with different filter parameters have been discussed [20]. Finally, the simulation and experimental results verify the theoretical analysis.

Chapter 5 gives a research summary of the achievement and future perspective for this thesis.

1.5. LIST OF PUBLICATIONS

A list of journal papers related to this thesis, which have been published or submitted, is given as:

J1. **M. Lu**, X. Wang, P.C. Loh, F. Blaabjerg, "Resonance Interaction of Multi-Parallel Grid-Connected Inverters with LCL Filter," *IEEE Trans. on Power Electron*. , vol. 32, no. 2, pp. 894–899, Feb. 2017.

J2. **M. Lu**, X. Wang, P.C. Loh, F. Blaabjerg, T. Dragicevic, "Graphical Evaluation of Time-Delay Compensation Techniques for Digitally Controlled Converters," *IEEE Trans. on Power Electron*., *Early access*, Mar. 2017.

J3. **M. Lu**, F. Blaabjerg, "Stability Identification and Robust Design of LCL-Filters for Grid-Connected Converters Considering Grid-Voltage Feedforward Regulator," *IEEE Trans. on Power Electron*., May 2017. (**Submitted**)

J4. **M. Lu**, F. Blaabjerg, X. Wang, "Interaction admittance based modeling of multi-paralleled grid-connected inverter with LCL-filter," *IEEE Trans. on Power Electron*., June 2017. (**Submitted**)

J5. T. Dragicevic, **M. Lu**, F. Blaabjerg, "Improved Model Predictive Control for High Voltage Quality in Micro-grid Applications," *IEEE Trans. on Power Electronics*. (**Submitted**)

J6. Z. Xin, X. Wang, Z. Qin, **M. Lu**, et al, "An Improved Second-Order Generalized Integrator Based Quadrature Signal Generator," *IEEE Trans. on Power Electronics.*, vol. 32, no. 2, pp. 894-899, Feb. 2017.

A list of conference papers related to this thesis, which have been published or submitted, is given as follows:

C1. **M. Lu,** X. Wang, P.C. Loh, F. Blaabjerg, "An analysis method for harmonic resonance and stability of multi-paralleled LCL-filtered inverters," in *Proc. of IEEE Power Electronics for Distributed Generation Systems* (*IEEE PEDG 2015*), Jun. 2015, pp 1-7.

C2. **M. Lu,** X. Wang, P.C. Loh, F. Blaabjerg, "Interaction and Aggregated Modeling of Multiple Paralleled Inverters with LCL Filter," in *Proc. of 2015 IEEE Energy Conversion Congress and Exposition* (*IEEE ECCE 2015*), Montreal, CA, Sep. 2015, pp. 1-7.

C3. **M. Lu**, X. Wang, F. Blaabjerg, et al, "Grid-voltage-feedforward active damping for grid-connected inverter with LCL filter," In *Proc. of 31th Annual IEEE Applied Power Electronics Conference and Exposition* (*IEEE APEC 2016*), Long Beach, CA, US, Mar. 2016, pp.1941-1946.

C4. **M. Lu**, Z. Xin, X. Wang, R. Beres, F. Blaabjerg, "Extended stable boundary of LCL-filtered grid-connected inverter based on an improved grid-voltage feedforward control," in *Proc. of 2016 IEEE Energy*

Conversion Congress and Exposition (IEEE ECCE 2016), Milwaukee, US, Sep. 2016, pp. 1-7.

C5. **M. Lu**, F. Blaabjerg, X. Wang, "Interaction admittance based modeling of multi-paralleled grid-connected inverter with LCL-filter," in *Proc. of 2016 IEEE 2nd Annual Southern Power Electronics Conference (IEEE SPEC 2016)*, Auckland, NZ, Dec. 2016, pp. 1-7.

C6. **M. Lu**, X. Wang, P.C. Loh, F. Blaabjerg, "Graphical Evaluation of Time-Delay Compensation Techniques for Digitally-Controlled Converters," in the *2017 IEEE Energy Conversion Congress and Exposition (IEEE ECCE 2017)*, Cincinnati, Ohio. (**Accepted**)

C7. **M. Lu**, F. Blaabjerg, "Stability Identification and Robust Design of LCL Filters for Grid-Connected Inverters Considering Grid-Voltage Feedforward Regulator," in the *2017 IEEE Workshop on Control and Modeling for Power Electronics (IEEE COMPEL 2017)*, Stanford University, Stanford, California, USA. (**Accepted**)

CHAPTER 2. STABILITY ANALYSIS AND ROBUST DESIGN OF LCL-FILTERS CONSIDERING GVFR

For the grid-connected inverters, feedforward control of grid voltage is commonly adopted to mitigate the current distortion caused by grid background voltages harmonics. This chapter reveals that, in an inductive weak grid, the Grid-Voltage Feedforward Regulator (GVFR) will significantly alter the converter stability. Then, a conservative LCL-filter design guideline to ensure the robustness against grid inductance variation is recommended. Beginning with the current loop analysis, where the system poles distribution are analytically studied in the *z*-domain, the critical frequency, as well as the control gain limit, is therefore calculated. Two frequency boundaries and three typical resonance frequency ranges are identified when the GVFR is added. The theoretical analysis is validated by experimental tests on a laboratory-scale prototype.

2.1. STABILITY ANALYSIS FOR A LCL-FILTERED INVERTER

In this study, current control implementation in stationary coordinates (the α-β frame) is assumed here [66]. Therefore, the conclusions obtained are applicable not only to the single-phase systems, but also to the per-phase control of multiphase systems.

2.1.1. MODELING

Figure 2-1 shows a voltage source converter connected to the grid through an LCL-filter. L_1 is the inverter-side inductor, C is the filter capacitor, and L_2 is the grid-side inductor, Z_g is the grid impedance. The inner resistances of L_1, L_2 and L_g are neglected considering the worst case. The grid current i is sampled and controlled through a linear controller with transfer function $G_c(s)$.

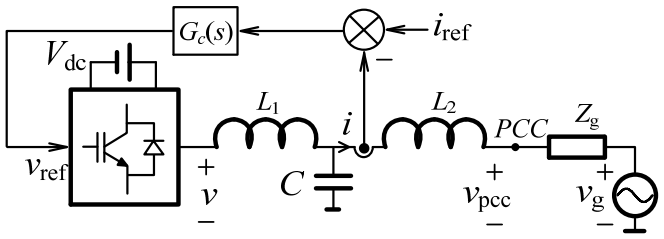

Figure 2-1 Circuit and current control diagram for a voltage source converter.

Digital control implementation is assumed, where the sampling is carried out synchronously with the converter switching. The control block diagram is represented in Figure 2-2, where the LCL-filter has been modeled in the continuous domain [42]. The digital control process will bring a total delay of $1.5 \cdot T_s$, including the computational delay z^{-1} and $0.5 \cdot T_s$ from discretization process (T_s represents the sampling period). A pure time delay suffices as a converter model as [66]

$$v = e^{-sT_d} \cdot v_{\text{ref}}, \qquad T_d = 1.5T_s \tag{2.1}$$

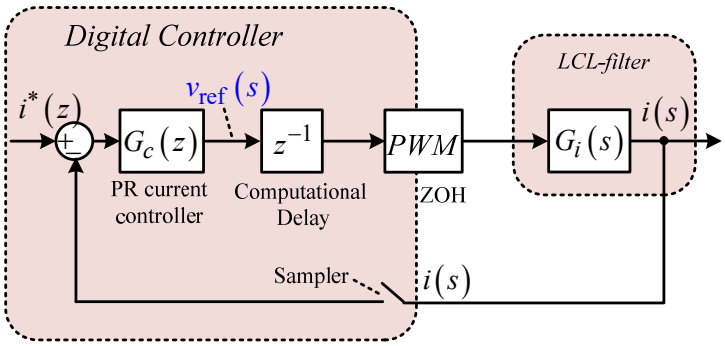

Figure 2-2 Implementation of digital controller in an LCL-filtered converter.

where v is the converter output voltage, v_{ref} is the controller output. The LCL-filtered system plant can be obtained where the function $G_i(s)$ for relating the v to the grid current i, as shown in Figure 2-1, can be derived as:

$$G_i(s) = \frac{i(s)}{v(s)} = \frac{1}{sL_1L_sC_f} \frac{1}{s^2 + \omega_r^2}, L_s = L_2 + L_g \tag{2.2}$$

where L_s is the sum of inductance L_2 and L_g . ω_r is the filter resonance frequency expressed as:

$$\omega_r = \sqrt{\frac{L_1 + L_s}{L_1L_sC_f}} \tag{2.3}$$

In (2.2), compared to L-filtered system, a resonant part is undesirably introduced in the LCL-filtered system, which may make the system oscillatory, even unstable [39]. By applying Zero-Order-Hold (ZOH) discretization scheme, the plant $G_i(s)$ can be transformed to the discrete expression $G_i(z)$ as shown in Figure 2-3 [42].

$$G_i(z)=\frac{\omega_r T_s\left[z^2-2z\cos(\omega_r T_s)+1\right]-\sin(\omega_r T_s)(z-1)^2}{\omega_r(L_1+L_s)(z-1)\left[z^2-2z\cos(\omega_r T_s)+1\right]} \tag{2.4}$$

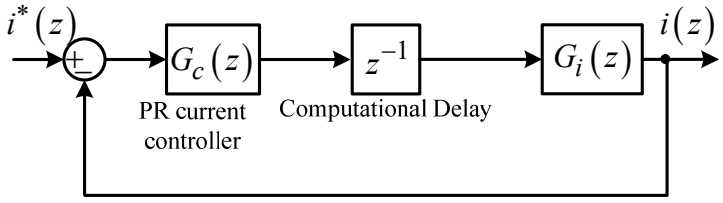

Figure 2-3 Circuit and control block diagram in the z-domain.

For the controller $G_c(s)$, the Proportional Resonant (PR) controller [68] is a common option for grid application, whose expressions in *s*-domain and *z*-domain are written in (2.5) and (2.6), respectively [42].

$$G_c(s)=K_p+\frac{K_i s}{s^2+\omega_b^2} \tag{2.5}$$

$$G_c(z)=K_p+\frac{K_i\sin(\omega_b T_s)}{2\omega_b}\frac{z^2-1}{z^2-2z\cos(\omega_b T_s)+1} \tag{2.6}$$

where ω_b is the fundamental frequency. The knowledge and design methods of the PR controller are well-known, and will not be discussed in detail [42] [68]. The open-loop transfer function $T_i(z)$ in (2.7) can finally be obtained through combining the expressions (2.4) and (2.6).

$$T_i(z)=\frac{G_c(z)}{\omega_r(L_1+L_s)}\cdot\frac{\omega_r T_s\left[z^2-2z\cos(\omega_r T_s)+1\right]-\sin(\omega_r T_s)(z-1)^2}{z\cdot(z-1)\cdot\left[z^2-2z\cos(\omega_r T_s)+1\right]} \tag{2.7}$$

2.1.2. POLES DISTRIBUTION

Since the open-loop transfer function is obtained, the system poles can be analyzed. From (2.6), the PR controller will introduce two poles, which are fixed at the fundamental frequency ω_b. These two poles will not influence system stability because they are fixed on the unit circle. Apart from them, another four open-loop poles z_1, z_2, z_3, z_4 can be identified, which includes two fixed poles at original point z_1 =0 and z_2=1, together with two resonant poles z_3, z_4 as shown in (2.8) and (2.9).

$$z_1=0,\ z_2=1 \tag{2.8}$$

$$z_{3,4} = \cos(\omega_r T_s) \pm j \cdot \sin(\omega_r T_s) = e^{\pm j\omega_r T_s} \tag{2.9}$$

To be emphatically pointed out, the resonant poles z_3, z_4 are the conjugate roots of equation $z^2 - 2z \cdot \cos(\omega_r T_s) + 1 = 0$, and can be expressed using exponential function with unity magnitude and phase changing with $\omega_r T_s$. The location and locus of these resonant poles can be plotted in a polar coordinate as shown in Figure 2-4, where the resonant poles z_3, z_4 track along the edge of unit circle.

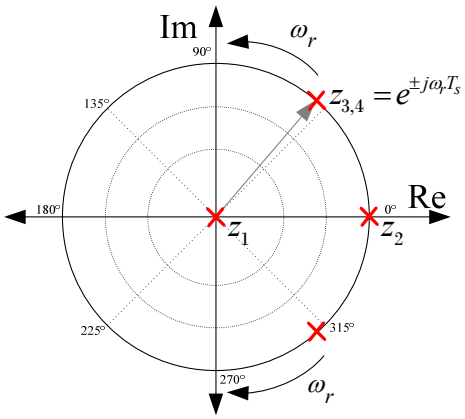

Figure 2-4 Poles location in a polar coordinate for the voltage source converter.

Although system stability is determined by the location of closed-loop poles instead of the open-loop ones, open-loop poles are starting points of closed-loop ones when the control gain K_p is equal to zero. Meanwhile, the open-loop poles $z_{3,4}$ are floating with $\omega_r T_s$. It indicates that system stability indirectly depends on the term $\omega_r T_s$ ($\omega_r T_s = 2\pi \cdot \omega_r / \omega_s$). Therefore, the ratio γ between the resonance frequency ω_r and sampling frequency ω_s, as expressed in (2.10), has significant impact on system stability.

$$\gamma = \frac{\omega_r}{\omega_s} \tag{2.10}$$

To verify the analysis above, Figure 2-5 shows the root loci with three ratios γ sets (γ_1=0.15, γ_2=0.24, γ_3=0.36) for recognizing the role of the ratio γ playing on the poles distribution. Obviously, the three plots have totally distinct poles distributions, hence, also different system stabilities.

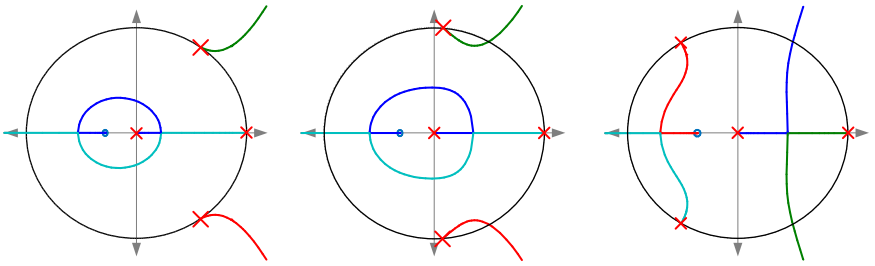

(a) *(b)* *(c)*

Figure 2-5 System root loci with different ratio γ: (a) γ_1=0.15; (b) γ_2=0.24; (c) γ_3=0.36.

Plot (a) with γ_1=0.15 presents an unstable system regardless of the proportional gain K_p, while plot (b) and (c) present a conditionally stable system if K_p is properly selected. Obvious differences exit for these three cases. To analyze these differences, the closed-loop transfer function is derived from $T_i(z)$ as

$$H(z)=\frac{T_i(z)}{1+T_i(z)} \tag{2.11}$$

The denominator polynomial $P(z)$ of the closed-loop transfer function $H(z)$ is expressed in (2.12). Then, the system poles are those roots of equation $P(z)$=0. It is worth to note that all the root loci plots track through the unit circle at the same point as they become unstable, which can be identified as $z_c = 1/2 \pm j\sqrt{3}/2$ [65]. This recognition can be confirmed using simple geometry and can then be used to develop a fundamental gain limitation for controller design [65]. Substituting z_c into $P(z)$=0, the proportional gain limitation $K_{p\_\lim}$ for the controller design, as written in (2.13), can be calculated.

$$\begin{aligned} P(z)=&\omega_r(L_1+L_t)\cdot z\cdot(z-1)\cdot\left[z^2-2z\cos(\omega_r T_s)+1\right] \\ &+K_p\left\{\omega_r T_s\left[z^2-2z\cos(\omega_r T_s)+1\right]-\sin(\omega_r T_s)(z-1)^2\right\} \end{aligned} \tag{2.12}$$

The limit value for the control gain can be derived from (2.12). From its expression, it is known that the $K_{p\_\lim}$ value is a function of term $\omega_r T_s$.

$$K_{p\_\lim}=\omega_r(L_1+L_t)\cdot\frac{1-2\cos(\omega_r T_s)}{\sin(\omega_r T_s)+\omega_r T_s\cdot(1-2\cos(\omega_r T_s))} \tag{2.13}$$

2.1.3. STABILITY ANALYSIS BASED ON K_{P_LIM} VALUE

According to (2.13), the relationship between the gain limit $K_{p\_\lim}$ and the ratio γ is plotted and shown in Figure 2-6, where the $K_{p\_\lim}$ value varies sign from negative to positive at $\omega_r=\omega_s/6 \approx 0.167\omega_s$. To be precise, the curve crosses over zero at the right

point where the numerator term 1-2cos($\omega_r T_s$) equalizes to zero. It means that a negative K_p gain is required to stabilize the converters with a resonance frequency below $\omega_s/6$. Regrettably, the K_p gains are always positive values, indicating that system will be unstable when the resonance frequency ω_r is less than $\omega_s/6$ regardless of the control gain value K_p. The system will be, on the other hand, conditionally stable only if the control gain is less than the limit calculated in (2.13).

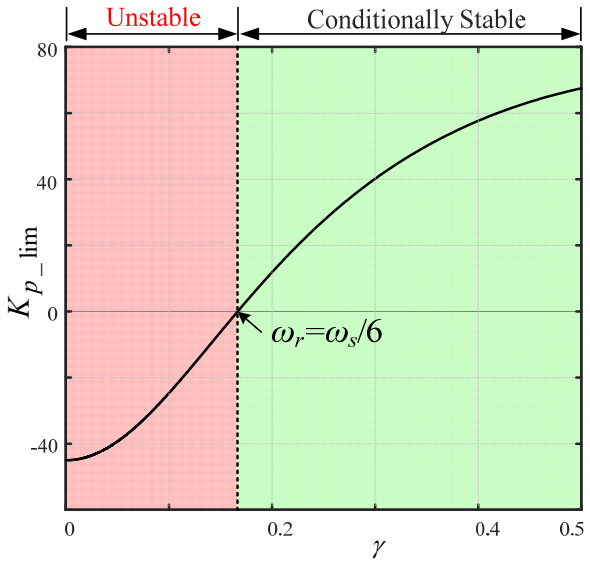

Figure 2-6 Relationship between Kp_lim and ratio γ for the voltage source converters with LCL-filter.

2.2. STABILITY IDENTIFICATION OF THE SITUATIONS WITH ADDITIONAL GVFR

Grid voltage feedforward control is widely used to improve grid-connected system dynamic performance and mitigate the grid voltage background harmonics. To evaluate the potential impact of GVFR on the system stability, continued analysis following the previous section on poles distribution will be executed next.

2.2.1. MODELING

Compared with Figure 2-1, an additional feedforward regulator $F(s)$ is inserted in Figure 2-7. For the regulator $F(s)$, [29] proposed a *Full -Feedforward* controller for LCL-filtered inverters, it improves the high-order harmonics mitigation performance compared to the traditional solution of applying a unity feedforward gain [39]. However, a high order controller is necessary, including a second order derivative term which is quite sensitive to noise [39]. It might lead to difficulties in practical

applications. In this study, a traditional solution with unity feedforward gain is considered $F(s)$ =1.

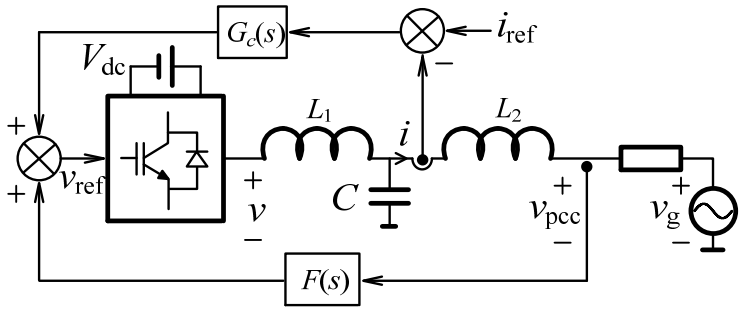

Figure 2-7 Circuit and block diagram with grid-voltage feedforward regulator.

The function for relating the converter output voltage v to the PCC voltage can be derived as:

$$G_{pcc}(s)=\frac{v_{pcc}(s)}{v(s)}=\frac{L_g}{L_1(L_2+L_g)C_f}\frac{1}{s^2+\omega_r^2} \tag{2.14}$$

Similarly, the continuous-domain transfer function can be transformed to the discrete-domain by applying ZOH discretization. The resulting function, notated in Figure 2-8 as $G_{pcc}(z)$, is given as follows.

$$G_{pcc}(z)=\frac{1-\cos(\omega_r T_s)}{L_1 C_f \omega_r^2}\frac{z+1}{z^2-2z\cos(\omega_r T_s)+1} \tag{2.15}$$

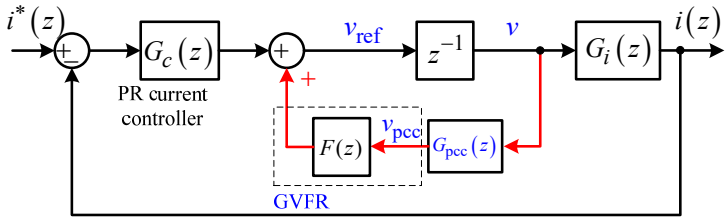

Figure 2-8 Control block diagram in z-domain with GVFR.

The blocks in Figure 2-8 can eventually be merged to give open-loop transfer function in (2.16). Compared to the transfer function in (2.7) without GVFR, (2.16) has the same form except the red-marked term. Therefore, it can be seen that an

additional GVFR $F(z)$ will modify the system characteristic polynomial, which certainly results in the system stability alteration.

$$T_i(z)=\frac{G_c(z)}{\omega_r(L_1+L_2+L_g)}\cdot\frac{\omega_r T_s\left[z^2-2z\cos(\omega_r T_s)+1\right]-\sin(\omega_r T_s)(z-1)^2}{(z-1)\cdot\left\{z\cdot\left[z^2-2z\cos(\omega_r T_s)+1\right]-k_a(z+1)(1-\cos(\omega_r T_s))\right\}} \tag{2.16}$$

where the k_a is a coefficient relating to the $F(z)$ with the expression as

$$k_a=\frac{L_g}{L_2+L_g}\cdot\frac{F(z)}{L_1\omega_r^2} \tag{2.17}$$

According to (2.17), when the grid inductance L_g is equal to 0, then k_a = 0, indicating that the GVFR will have no impact on the inverter system stability under stiff grid conditions. On the other hand, if the grid inductance L_g is a non-zero value, i.e., the power system is weak, in some cases, varying within a large range [69]. The situation is particularly critical in rural areas where the distributed generation plants are connected due to many good natural resources, like solar or wind [69]. Then, the system stability is altered if the GVFR is added, and then do need more investigation.

2.2.2. OPEN-LOOP POLES ANALYSIS THROUGH JURY'S CRITERION

Fundamentally, the characteristic polynomial of (2.16), which is expressed $D(z)$ as (2.18), plays a crucial role in the poles distribution. Because the roots of $D(z)$ are exactly the system poles, including a fixed one z_1=1determined by term (z-1) and other three poles are determined by the rest part, written as $D_1(z)$ in (2.19).

$$D(z)=(z-1)\cdot\left\{z\cdot\left[z^2-2z\cos(\omega_r T_s)+1\right]-k_a(z+1)(1-\cos(\omega_r T_s))\right\} \tag{2.18}$$

To calculate the roots of $D_1(z)$ and analyze the distribution of the poles, the Jury's criterion [70] is adopted, $D_1(z)$ is rewritten as the descending power series.

$$\begin{aligned} D_1(z) &= z\cdot\left[z^2-2z\cos(\omega_r T_s)+1\right]-k_a(z+1)(1-\cos(\omega_r T_s)) \\ &= a_0\cdot z^3+a_1\cdot z^2+a_2\cdot z+a_3 \end{aligned} \tag{2.19}$$

where the coefficients can be written as:

$$\begin{cases} a_0 = 1 \\ a_1 = -2\cdot\cos(\omega_r T_s) \\ a_2 = 1-k_a+k_a\cdot\cos(\omega_r T_s) \\ a_3 = k_a\cdot\cos(\omega_r T_s)-k_a \end{cases} \tag{2.20}$$

Then the Jury table is constructed as follows:

Table 2-1 Jury table for voltage source converter considering GVFR

Row	z^0	z^1	z^2	z^3
1	a_3	a_2	a_1	a_0
2	a_0	a_1	a_2	a_3
3	b_2	b_1	b_0	-

The first row is constructed of the polynomial coefficients in decreasing order while the second row is the first row in reverse order and conjugated [74]. The third row of Table 2-1 is calculated as

$$b_2 = \begin{vmatrix} a_3 & a_0 \\ a_0 & a_3 \end{vmatrix}, b_1 = \begin{vmatrix} a_3 & a_1 \\ a_0 & a_2 \end{vmatrix}, \; b_0 = \begin{vmatrix} a_3 & a_2 \\ a_0 & a_1 \end{vmatrix} \tag{2.21}$$

The table can be expanded in this manner until a row containing only one non-zero element is reached [74]. In short, the polynomial $D_1(z)$ has all three roots inside of the unit circle if and only if the following requirements are met:

- $|a_3| < a_0$;
- $D_1(z)|_{z=1} > 0$;
- $D_1(z)|_{z=-1} < 0$;
- $|b_2| > |b_0|$.

(2.22)

From (2.20) and (2.21), the elements in Table 2-1: $a_0 \ldots a_3$, $b_0 \ldots b_2$ are the functions of k_a and ω_r, both of which are dependent on the feedforward gain $F(z)$ and the LCL-filter parameters. Consequently, the selection of the feedforward $F(z)$ and filter parameters would make a difference on the system stability.

As mentioned earlier, the traditional feedforward solution applies a unit feedforward gain $F(z) = 1$, hence, different sets of filter parameters and resonance frequencies might have totally different system performance and stability characteristics.

2.2.3. BOUNDARY VALUES FOR FEEDFORWARD GAIN

It has been pointed out that different F values will result in different system characteristics. Although F is a fixed gain for traditional solution, the ranges can be identified through obtaining the boundaries. Two boundary values F_a and F_b can be derived by solving the inequalities in (2.22) to divide the whole stability region into three parts, which will be discussed in the following paragraph. The expressions of F_a and F_b are given as

$$F_a = \frac{L_1 + L_2 + L_g}{L_g} \tag{2.23}$$

$$F_b = \frac{L_1 + L_2 + L_g}{L_g} \cdot \frac{2\cos(\omega_r T_s) + 1}{1 - \cos(\omega_r T_s)} \tag{2.24}$$

From the expressions above, F_a is a constant value whereas F_b is related to the filter resonance frequency ω_r. The F_b value has three possible options: 1) F_b is equal to or greater than F_a; 2) F_b is greater than 0, but smaller than F_a; and 3) F_b is less than 0. These three possibilities are shown in Figure 2-9, where two special F_b boundary values need more attention: 1) $\boldsymbol{F_a}$: If $\omega_r = \omega_s/4$, the term $\omega_r T_s$ is equal to $\pi/2$, then $F_b = F_a$; 2) **0**: If $\omega_r = \omega_s/3$, the term $2\cos(\omega_r T_s) + 1 = 0$, then $F_b = 0$.

Therefore, the whole resonance frequency range can also be artificially divided into three regions according to which range in Figure 2-9 F_b is located: 1) $\omega_r \in (0, \omega_s/4)$; 2) $\omega_r \in (\omega_s/4, \omega_s/3)$; 3) $\omega_r \in (\omega_s/3, \omega_s/2)$.

Figure 2-9 Three possible value ranges for F_b.

2.2.4. STABILITY IDENTIFICATION FOR DIFFERENT RESONANCE FREQUENCIES RANGES

As mentioned earlier, the open-loop poles location is dependent on both the LCL-filter resonance frequency and the feedforward gain F. Following the analysis, Table 2-2, 2-3, 2-4 give a comprehensive picture on how the ω_r and the gain F decide the open-loop unstable poles.

1) $\omega_r \in (0, \omega_s/4)$

In this range, $0 < F_a < F_b$. Figure 2-10 plots the F_a and F_b value varying with the grid inductance L_g according to (2.23) and (2.24), where both F_a and F_b have individual limit values. With the increasing L_g value, F_a is approaching to 1 while F_b is approaching to F_{b_Lim} as given in (2.25), because the LCL-filter resonance frequency ω_r is approaching to ω_{L_1C} when the grid inductance is large enough.

$$F_{a\_Lim} = 1, \quad F_{b\_Lim} = \frac{2\cos(\omega_{L_1C} T_s) + 1}{1 - \cos(\omega_{L_1C} T_s)} \tag{2.25}$$

where $\omega_{L_1C} = \sqrt{1/L_1C}$.

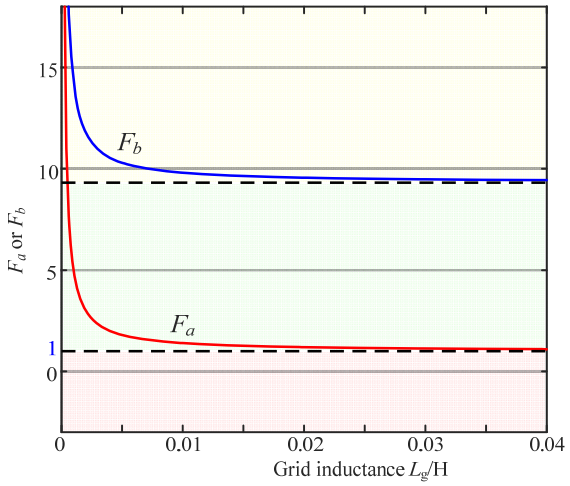

Figure 2-10 F_a and F_b value under $\omega_r \in (0, \omega_s/4)$.

Applying the Jury's criterion again, Table 2-2 gives the open-loop poles number outside of unit circle in the complex plane. For traditional feedforward solution, F is equal to 1, which belongs to the range [0, F_a]. The number of open-loop unstable poles is zero, which means, originally, these poles are located inside the unit circle.

Table 2-2 Poles Distribution for $0< \omega_r < \omega_s/4$

$0< \omega_r < \omega_s/4$				
F	$(-\infty, 0)$	$[0, F_a]$	$(F_a, F_b]$	$(F_b, +\infty)$
P	2	0	1	3
Status	-	stable	unstable	unstable

The Nyquist Stability Criterion (NSC) criterion indicates that if P is an odd number, the system will certainly be unstable. For instance, $P = 1$ or 3, the system is unstable. To verify the analysis above, Figure 2-11 plots the open-loop and closed-loop poles distribution varying with the grid inductance L_g, respectively, where the closed-loop poles are marked with crosses while the open-loop poles are marked with the crosses inside the circle. For the open-loop poles, the GVFR ensures no open-loop poles outside of the unit circle: a pole (z=1) is fixed; besides, two resonant open-loop poles are pulled inside of the unit circle. This is in agreement with the number P given in Table 2-2. Furthermore, this open-loop poles map also reveals that the GVFR offers a damping contribution to the resonance, the same conclusion is presented in [39] as well.

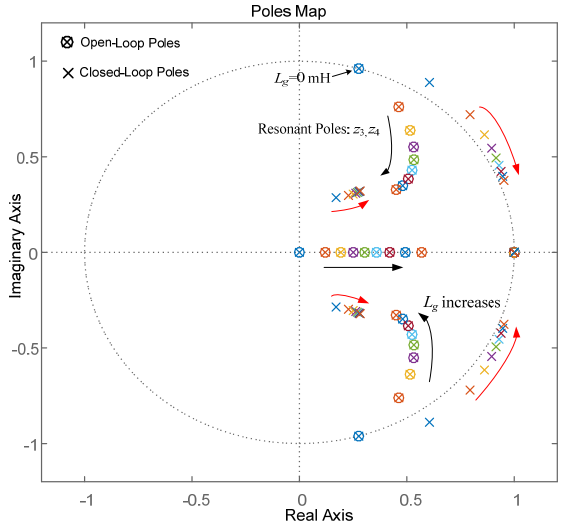

Figure 2-11 Open loop and closed loop poles maps under $\omega_r \in (0, \omega_s/4)$.

$$K_p = \omega_u \cdot (L_1 + L_2) \tag{2.26}$$

For the closed-loop poles map, the control gain K_p is selected as (2.26) according to the current loop bandwidth ω_u and the grid-side and inverter-side inductance L_1 and L_2. As presented in Figure 2-11, such a selection makes two closed-loop poles outside of unit circle, leading to system instability. The fundamental reason is that the studied range is close to the critical frequency, resulting in limited K_p choices according to Figure 2-6. Nonetheless, the additional GVFR makes the poles approaching to the circle brink, once again demonstrating its damping effect on system stability.

2) $\omega_r \in (\omega_s/4, \omega_s/3)$

Figure 2-12 plots the F_a and F_b values varying with the grid inductance L_g, where the whole plane is divided into two parts by $\omega_r = \omega_s/4$: 1) Left plane with $F_a > F_b$; 2) Right plane with $F_a < F_b$, which has been discussed. The curve F_a intersects with the curve F_b at the point $\omega_r = \omega_s/4$. Table 2-3 presents the results corresponding to Table 2-2. For traditional feedforward solution, F is equal to 1, belonging to the range [0, F_b] or (F_b, F_a]. It depends on whether F_b is larger than 1 or not. A conservative design is to have the limit value F_{b_Lim} larger than 1. Then, all the F_b in this range will be above 1. The number of open-loop unstable poles is zero, which means, originally, these poles are located inside the unit circle.

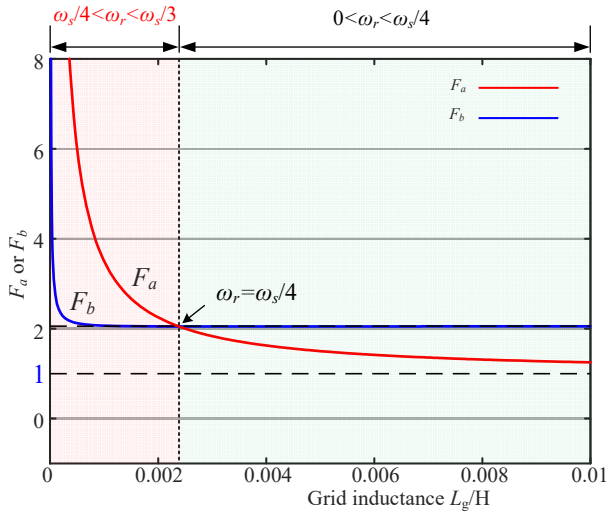

Figure 2-12 F_a and F_b value under $\omega_r \in (\omega_s/4, \omega_s/3)$.

Table 2-3 Poles Distribution for $\omega_r \in (\omega_s/4, \omega_s/3)$

$\omega_s/4 < \omega_r < \omega_s/3$				
F	$(-\infty, 0)$	$[0, F_b]$	$(F_b, F_a]$	$(F_a, +\infty)$
P	2	0	2	3
Status	-	stable	-	unstable

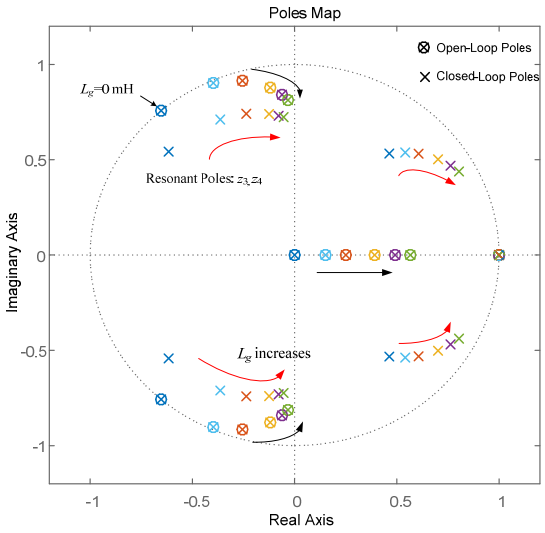

Figure 2-13 Open loop and closed loop poles maps under $\omega_r \in (\omega_s/4, \omega_s/3)$.

As anticipated, Figure 2-13 shows that there is no open-loop pole outside of the unit circle in this frequency range. Different from the poles movement in Figure 2-11, here, the closed-loop poles track directly inside the unit circle, and the increasing grid inductance value does not push the poles outside the unit circle. It means the GVFR stabilizes the current loop, moreover, improves the system robustness to the grid inductance variation. In this case, no additional active damping scheme is required to damp the resonance because all the poles are inside the circle.

2) $\omega_r \in (\omega_s/3, \omega_s/2)$

In this range, the F_b value belongs to $F_b<0<F_a$. As shown in Figure 2-14, F_a and F_b approach their limit values from positive and negative infinity, respectively. Accordingly, Table 2-4 gives the number of the open-loop poles outside the unit circle. If the feedforward gain $F = 1$, regrettably, two unstable poles appear in such a case. In other words, the system tends to be unstable if the resonance frequency ω_r is higher than $\omega_s/3$. Figure 2-15 demonstrates the stability status with varying grid inductor, where (a) has only the current loop without GVFR whereas (b) equips the traditional feedforward $F = 1$.

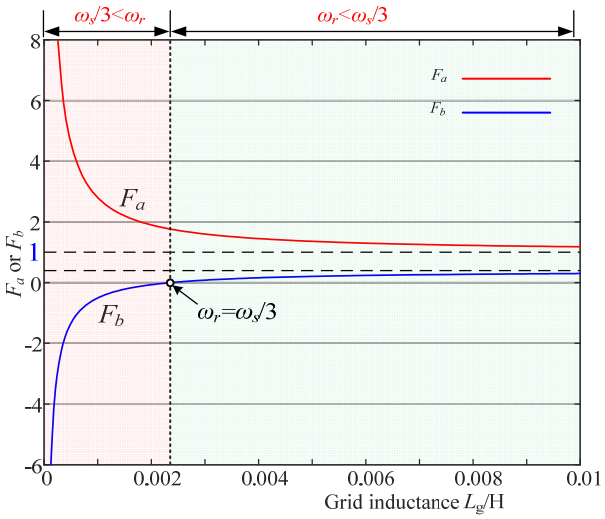

Figure 2-14 F_a and F_b value under $\omega_r \in (\omega_s/3, \omega_s/2)$.

In Figure 2-15 (a), although the resonance frequency ω_r decreases according to (2.3) with the grid inductance increasing, the poles are still located inside the unit circle because ω_r is beyond the critical frequency. In contrast, the additional GVFR pushes these poles outside the unit circle in this frequency range as shown in Figure 2-15 (b), including open-loop poles and closed-loop poles. The poles distributions reveal that GVFR will destabilize the system if the resonance frequency is beyond $\omega_s/3$. Particular attention should be paid here while designing the LCL-filter.

Table 2-4 Poles Distribution for $\omega_s/3< \omega_r < \omega_s/2$

$\omega_s/3< \omega_r < \omega_s/2$				
F	$(-\infty,F_b)$	$[F_b, 0]$	$(0, F_a]$	$(F_a, +\infty)$
P	2	0	2	3
Status	-	-	-	unstable

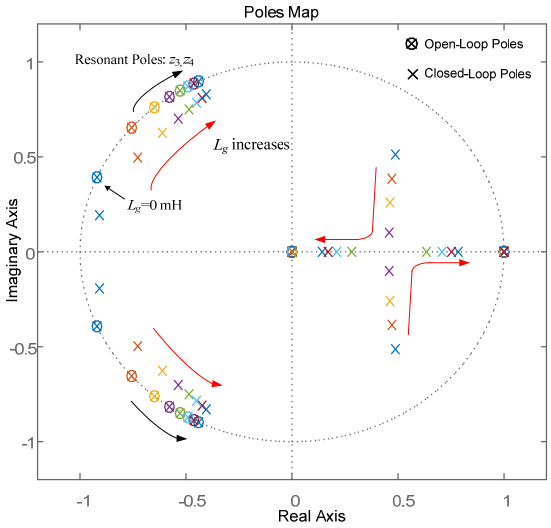

(a)

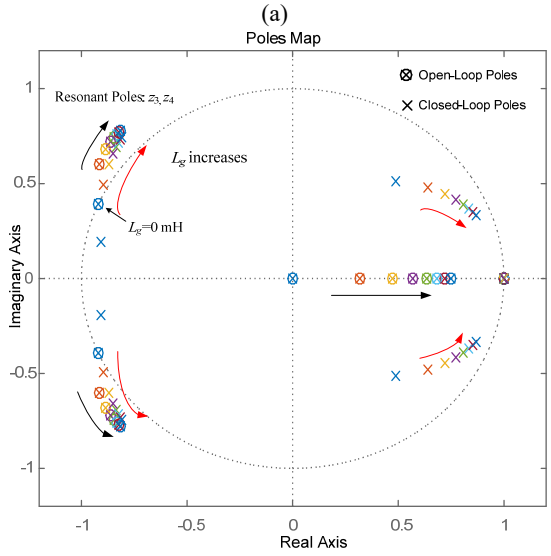

(b)

Figure 2-15 Open loop and closed loop poles maps under $\omega_r \in (\omega_s/3, \omega_s/2)$: (a) without GVFR; (b) with GVFR.

2.3. ROBUST DESIGN GUIDELINE FOR LCL FILTER

As studied in previous section, different filter parameters will significantly alter the system stability. In this part, an LCL-filter design recommendation for grid-connected applications considering the GVFR is discussed.

2.3.1. DETERMINATION OF FILTER INDUCTANCE L_1 AND L_2

For the ripple in the filter inductor, the larger the inductance is, the smaller ripple exists in the filter and the lower limit is determined by the current ripple requirement [75]. However, a large inductance will slow the system dynamic response, increase volume and cost, also lead to a greater voltage drop on the inductor as well. Therefore, the total value of inductance ($L_T = L_1 + L_2$) should be less than 0.1 pu to limit the ac voltage drop during operation [19]. Otherwise a higher dc-link voltage will be required to guarantee current controllability, which will result in higher switching losses [75]. The maximum value for the total inductance can be written as

$$L_{T\_\max} \le 10\% \cdot \frac{(v_g / \sqrt{3})^2}{\omega_0 \cdot S_0 / 3} \tag{2.27}$$

For two-level voltage source inverter, the maximum current ripple at the output of dc/ac inverter is [71]

$$\Delta I_{L\max} = \frac{2V_{DC}}{3L_1}(1-m)\cdot m \cdot T_s = \frac{V_{DC}}{6 f_{sw} L_1}, \text{ when } m = 0.5 \tag{2.28}$$

Calculate the minimum limitations of inductance L_1 [71]:

$$L_1 \ge \frac{V_{DC}}{6 f_{sw} \Delta I_{L\max}} \tag{2.29}$$

A 30% ripple of the rated current for the design parameters is assumed here, as expressed in

$$\Delta I_{L\max} = 0.3 \cdot I_{rated} = 0.3 \cdot \frac{\sqrt{2} \cdot S_0}{\sqrt{3} \cdot v_g} \tag{2.30}$$

Substituting (2.30) into (2.29), the minimum value of inverter-side inductance L_1 can be obtained as [71]

$$L_1 \ge \frac{5 V_{DC} v_g}{3\sqrt{6} f_{sw} S_0} \tag{2.31}$$

For grid-side inductance L_2, an index N is defined as the magnitude ratio of the inverter-side current ripple to the grid-side current ripple at the switching frequency [72].

$$N = \left|\frac{i_i}{i_g}\right| = \frac{H_i}{H_g} = \left|L_2 C\omega_{sw}^2 - 1\right| \tag{2.32}$$

where H_i and H_g are expressed as (2.33). The greater the N value is, the less harmonics exist in the grid-side current. N is determined by the switching frequency ω_{sw}, the inductance L_2 and filter capacitance C [72]. L_2 can be selected once the filter capacitance C is fixed according to (2.32). Usually, N is greater than 20.

$$H_i = \left|\frac{L_2 Cs^2 + 1}{L_1 L_2 Cs^3 + L_T s}\right|_{s=j\omega_{sw}}, H_g = \left|\frac{1}{L_1 L_2 Cs^3 + L_T s}\right|_{s=j\omega_{sw}} \tag{2.33}$$

$$L_2 = \frac{N+1}{C \cdot \omega_{sw}^2} \tag{2.34}$$

Moreover, it is necessary to check if the sum of $L_1$and L_2 is lower than the limit value in (2.27).

2.3.2. SELECTION OF FILTER CAPACITANCE

The maximum limitation of filter capacitance C can be estimated by the maximum fundamental reactive power [19]

$$C_{\max} \le \beta \cdot \frac{S_0 / 3}{\omega_0 \cdot (v_g / \sqrt{3})^2} \tag{2.35}$$

where S_0 is the rated power capacity, β is device fundamental reactive power index, expresses as the ratio of the acceptable maximum device fundamental reactive power to the rated power capacity, and usually set to 5% in the design [19]. The capacitor voltage is substituted by v_g for numerical approximations.

2.3.3. ROBUST DESIGN GUIDELINE FOR FILTER RESONANCE FREQUENCY

In a weak power system, the uncertain grid inductor L_g lead to varying LCL resonance frequencies for the voltage source inverters. According to (2.3), the minimum and maximum resonance frequencies can be calculated as

$$\omega_{r\_\min} = \omega_r\big|_{L_g\to\infty} = \sqrt{\frac{1}{L_1 C}}, \tag{2.36}$$

$$\omega_{r\_\max} = \omega_r\big|_{L_g=0} = \sqrt{\frac{L_1+L_2}{L_1 L_2 C}}. \tag{2.37}$$

Already concluded in the previous section, for the investigated system with GVFR, resonance frequency over the boundary $\omega_s/3$ would cause undesirable instability due to two unstable poles outside the unit circle. Hence, a conservative design for resonance frequency ω_r is to ensure the maximum ω_r below the boundary $\omega_s/3$. Then, the resonance frequency will never cross the $\omega_s/3$ despite variation of grid inductor.

On the other hand, the damping effect has already been demonstrated in the range (0, $\omega_s/4$). Despite that, the system with GVFR is still likely to be unstable because such a range is quite close to the critical frequency, which is equal to $\omega_s/6$. For instance, a non-zero grid inductance may make the resonance frequency below the critical frequency. If the minimum value ω_{r_min} is above $\omega_s/6$, then the real resonance frequency will be above the critical frequency. Moreover, the GVFR will provide damping effect on the range ($\omega_s/6$, $\omega_s/4$). In a nutshell, to guarantee system robustness to grid inductance variation, $\omega_{r\_\min} > \omega_s/6$ is recommended. In summary, the filter resonance frequency can be selected as

$$\frac{\omega_s}{6} < \omega_{r\_\min};\quad \omega_{r\_\max} < \frac{\omega_s}{3} \tag{2.38}$$

Figure 2-16 plots the selectable area of filter capacitance C, which is restricted by the equation (2.38) and maximum capacitance (2.35).

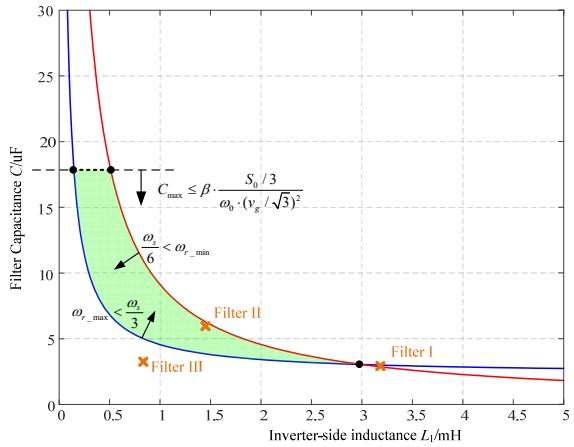

Figure 2-16 Selectable area of filter capacitance C.

2.4. EXPERIMENTAL VERIFICATION

For verification, a laboratory-scale prototype inverter with LCL-filter of Figure 2-1 is built to verify the analysis. Its physical layout and parameters used are given in Figure 2-17 and Table 2-5, respectively. The controller is implemented in a dSPACE system. A 15 kW programmable grid emulator is used to offer selectable grid voltage, and the grid impedance is replaced by an external inductor. Three different sets of LCL-filter parameters are used and given in Table 2-5 to verify the analysis of different frequency regions, namely region 1 (0, $\omega_s/4$), region 2 ($\omega_s/4$, $\omega_s/3$), and region 3 ($\omega_s/3$, $\omega_s/2$).

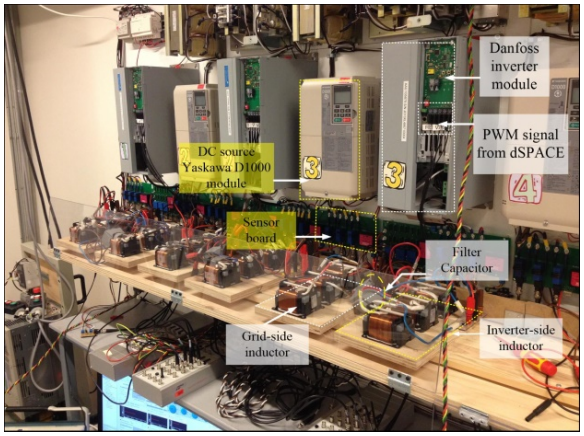

Figure 2-17 Experimental setup photo.

At first, the parameters of Filter I are chosen, which is actually outside the robust area set in Figure 2-16. Because its resonance frequency is close to the critical frequency. Here, the sampling frequency is selected as 20 kHz, whose critical frequency equalizes to 3.33 kHz. Figure 2-18 (a) shows the experimental waveforms, where the system is originally stable in a stiff grid. Obviously, such a system is not robust to grid inductance variation. As shown in Figure 2-18 (b), the system becomes undesirably oscillatory when the grid impedance is inserted. An external grid inductance L_g is added to emulate the weak power system. Figure 2-18 (c) shows the result that the system returns to stable if the GVFR is enabled. It demonstrates the damping effects of the feedforward scheme on the LCL filter resonance for the region 1 case, which has been concluded in previous section.

Following the above case, Figure 2-19 shows the experimental waveforms with the Filter II parameters, located right inside the robust area in Figure 2-16. Such a system should be more robust to different grid conditions. All resonance frequencies in this range are above the critical frequency, hence the system can work stable without damping. The sampling frequency is selected as 10 kHz, whose critical

frequency equalizes to 1.67 kHz. To verify the damping effect, the dynamic responses are compared. A step change in the reference from 2.5 to 5A is set to demonstrate the dynamic performance and potentially excite any resonance that may occur. Figure 2-19 (a) shows the experimental response for the case without GVFR. The system is clearly still quite stable, but has insufficient damping, as displayed by the slight oscillatory response just after the transient step. Comparatively, Figure 2-19 (b) shows the result for the case with GVFR. It is clear that almost no oscillations can be observed during the transient, which confirms the theoretical analysis.

Table 2-5 Experiment Parameters

Nominal System Parameters		
Rated capacity	S_0	10kVA
Grid frequency	f_0	50 Hz
DC-link voltage	V_{dc}	500V
Switching frequency	f_{sw}	10 kHz
Grid voltage (p-p)	v_g	300Vrms
Parameters of Filter I		
Converter-side inductor	L_1	3.2mH
Filter capacitor	C	3μF
Grid-side inductor	L_2	0.8mH
Grid inductance	L_g	1.5mH
Resonance frequency	f_r	2.51kHz
Parameters of Filter II		
Converter-side inductor	L_1	1.5mH
Filter capacitor	C	6μF
Grid-side inductor	L_2	0.8mH
Grid inductance	L_g	0.8mH
Resonance frequency	f_r	2.34kHz
Parameters of Filter III		
Converter-side inductor	L_1	0.8mH
Filter capacitor	C	3μF
Grid-side inductor	L_2	0.8mH
Grid inductance	L_g	0.8mH
Resonance frequency	f_r	3.98kHz

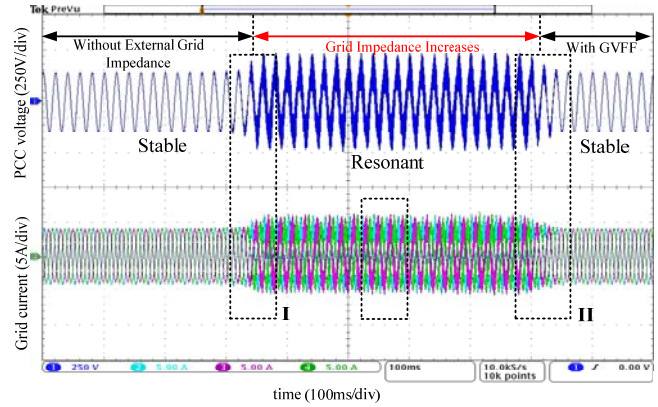

(a)

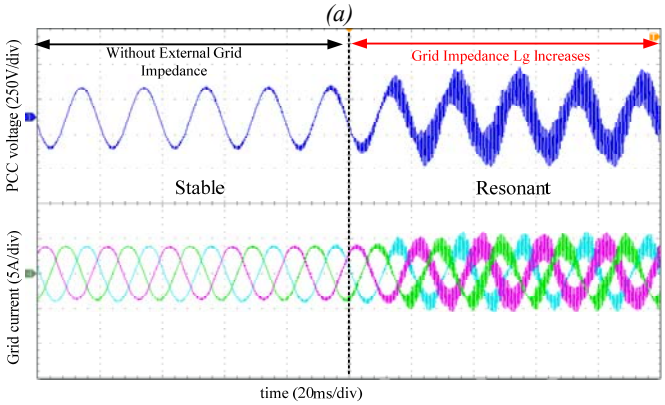

(b) I

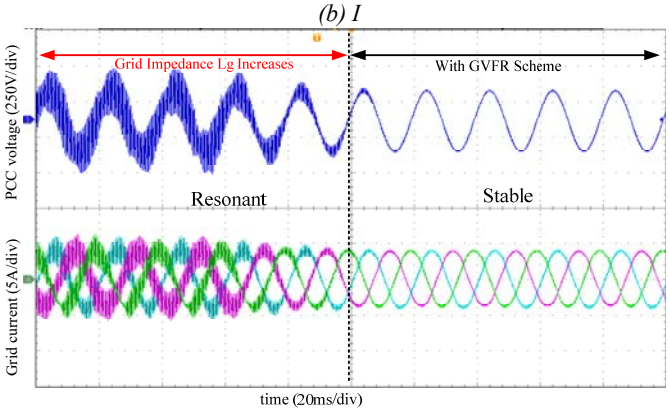

(c) II

Figure 2-18 Measured grid current and PCC voltage waveforms for frequency region 1 (a) full scale, (b) grid impedance makes system unstable, (c) the GVFR scheme is added.

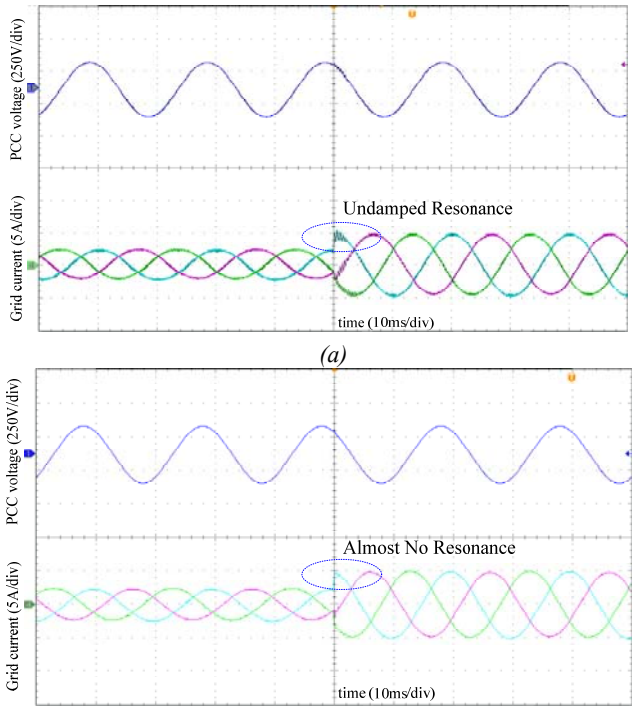

Figure 2-19 Measured grid current and PCC voltage waveforms for frequency region 2 (a) grid current step change from 2.5A to 5A without GVFR; (b) grid current step change from 2.5A to 5A with GVFR.

Similar experiments are carried out for the Filter III parameters, which is also outside the robust area. Note that the system will be stable without additional damping for this frequency range. Figure 2-20 shows the experimental waveforms when the GVFR scheme is employed in this situation. This is in agreement with the poles map shown in Figure 2-15, where the resonant poles are located just outside the unit circle and, thus, describe a system that is underdamped and unstable.

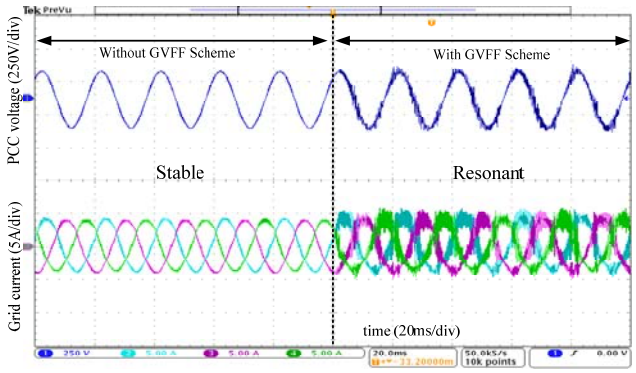

Figure 2-20 Measured grid current and PCC voltage waveforms for frequency region 3 with unit proportional GVFR scheme.

2.5. SUMMARY

This chapter comprehensively discusses the stability issue of grid-connected inverters with LCL-filter considering the GVFR. Beginning with poles distribution analysis for current loop, this chapter studies the impacts concerning GVFR using the similar method. It has been revealed that, in a weak power system, the GVFR will significantly alter the system stability. Based on the stability analysis in different frequency ranges, this chapter recommends a robust design for LCL-filter in the grid-connected application. Through theoretical and experimental verification, the parameters designed inside the robust area are more robust to the variation of grid inductance.

CHAPTER 3. GRAPHICAL EVALUATION OF TIME-DELAY COMPENSATION TECHNIQUES [46]

For a converter using the digital processor for control system, the digital time delay is a main reason to reduce the system bandwidth, leading to a relatively slow dynamic or even unstable operation [46]. To alleviate the negative impacts of digital delays, various compensation schemes have been proposed [44]-[51]. They can be divided into two basic categories: the model-based methods and the model-free ones. The former requires the detailed and accurate modeling while the latter is independent on the model accuracy [46]. This chapter begins with showing a graphical explanation of several model-free compensation approaches, where their compensation performances and operating principles are directly compared and revealed [46]. Based on the comparison results, an improved scheme with strong compensation ability is presented in this thesis. It provides satisfactory phase-lag compensation performance. Finally, the theoretical comparison of these studied compensation methods are verified through simulation and experimental tests on a grid-connected inverter with LCL-filter.

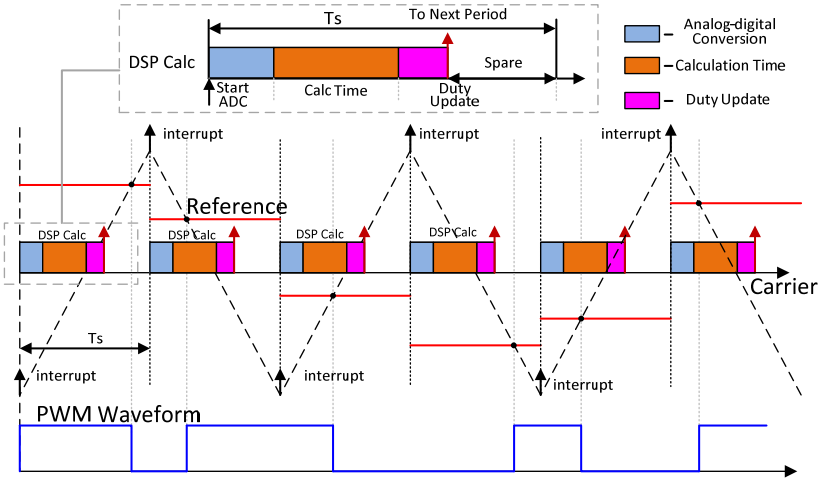

Figure 3-1 Practical implement of the control in a digital controller [46].

3.1. DIGITAL DELAY GENERATION IN A DIGITAL CONTROLLER

3.1.1. REASON OF TIME DELAYS

Digital processors are increasingly employed in the control systems to flexibly execute the control algorithm and modulation process [46]. Figure 3-1 presents the detailed control and modulation process during a complete sampling period, where the reference is frozen at the beginning of each sampling period and then compared against a triangular carrier ramp using a digital comparator [46]. A nonzero time period is necessary to implement the control and obtain a new duty cycle during the practical control process.

Instead of loaded right after the control calculation, the updated duty cycle is loaded at the start of next control period to avoid the inaccurate duty cycle update [46]. Therefore, an exact one-control-period delay is brought into the control system. Although the delay time is relatively short in a high-speed processor, it always equalizes to one control period and can be expressed as z^{-1}[46].

3.1.2. DETAILED PRESENTATION OF DIGITAL DELAYS

To concisely present the process above, Figure 3-2 presents an alternative graphical representation. In this figure, the $r(k)$ is the ideal modulation waveform while $s(k)$ is the real signal considering the one-sample delay [46]. To highlight the delay, the $s(k)$ lags one control period behind the $r(k)$ and the relationship between these two signals can be expressed as [46]

$$s(k) = r(k-1) = r(k) \cdot z^{-1} \tag{3.1}$$

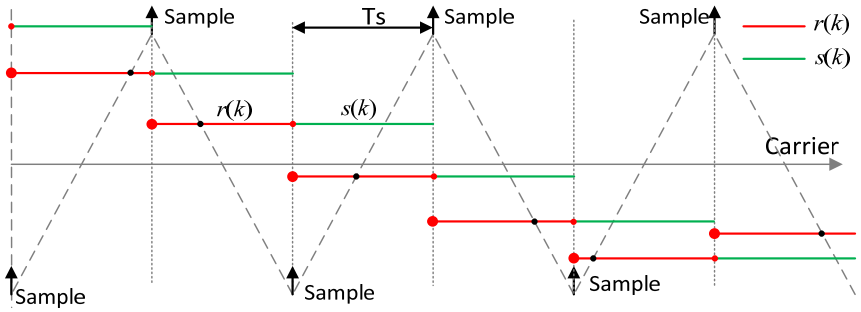

Figure 3-2 The graphical presentation of the digital delay [46].

3.2. EVALUATION AND COMPARISON OF COMPENSATION METHODS

3.2.1. EVALUATION AND COMPARISON PRINCIPLE

Theoretically, a pure one step lead term $z^{\wedge 1}$ can fully compensate the delay mentioned above, regrettably, such term requires the data in the future step which is not accessible in a practical digital processor [46]. To emulate the term $z^{\wedge 1}$, the measurement one fundamental period ago is utilized in [50]. This method, however, will bring additional 20ms (for 50Hz as fundamental frequency) delay time and further worsen system dynamic and stability [46]. Besides, many other methods are proposed in [44]-[51] with the purpose to replace the pure phase lead element $z^{\wedge 1}$ using specific equations [46].

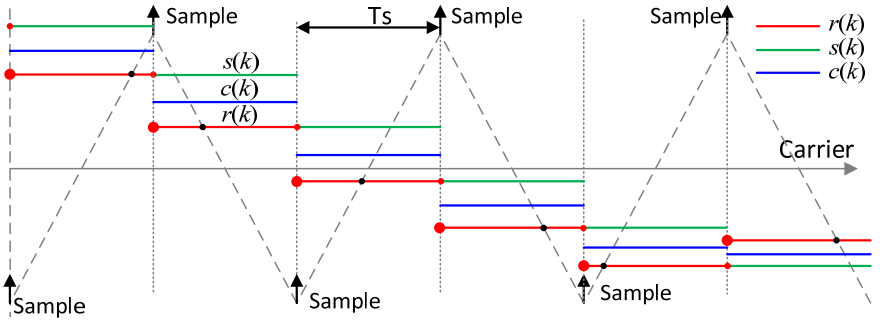

Figure 3-3 The graphical representation of the principle of delay compensation method [46].

To estimate and evaluate the proximity of the signal $c(k)$ to the signal $r(k)$, a graphical-based method is then introduced [46]. As shown in Figure 3-3, if $c(k)$ is geometrically closer to $r(k)$ than $s(k)$, it indicates that the equivalent phase of $c(k)$ is closer to the ideal signal $r(k)$ and the phase lag is then compensated and reduced, which demonstrates its compensation ability [46].

3.2.2. EVALUATION OF THE DIFFERENT COMPENSATORS [46]

3.2.2.1 Linear Predictor

A so-called *linear predictor* is a well-known method to compensate such time delays whose principle is based on the linear extrapolation technique [44] [46]. As stated, if the delay to be compensated is T_d, the discrete transfer function $L(z)$ can be written as [46]

$$L(z) = 1 + \frac{T_d}{T_s} - \frac{T_d}{T_s} \cdot z^{-1} \tag{3.2}$$

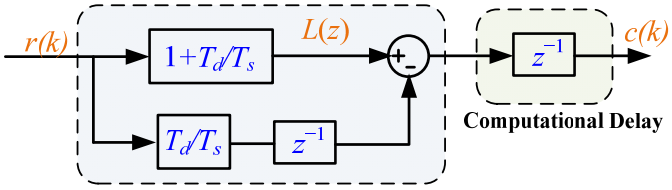

Figure 3-4 Block diagram of the linear predictor L(z) [46].

Figure 3-4 presents the block diagram of the linear predictor where the $r(k)$ is the original signal while the $c(k)$ is the compensated signal through the compensator [46]. The expression of $c(k)$ can be written as [46]

$$\frac{c(k)}{r(k)} = (1+\frac{T_d}{T_s}-\frac{T_d}{T_s}\cdot z^{-1})\cdot z^{-1} = (1+\frac{T_d}{T_s})\cdot z^{-1}-\frac{T_d}{T_s}\cdot z^{-2} \tag{3.3}$$

$$c(k) = (1+\frac{T_d}{T_s})\cdot r(k-1)-\frac{T_d}{T_s}\cdot r(k-2) \tag{3.4}$$

The equation (3.4) is still valid if both sides of this equation are multiplied by the same variable T_s, as expressed in (3.5) [46]. The compensation process of linear predictor can be explained during every sampling step through the relationship of area A_0, A_1, A_2, A_3 as illustrated in Figure 3-5 [46].

$$\underbrace{c(k)\cdot T_s}_{A3} = \underbrace{r(k-1)\cdot T_s}_{A0} - \overbrace{\underbrace{\frac{T_d}{T_s}\cdot\{r(k-2)-r(k-1)\}\cdot T_s}_{A1}}^{A2} \tag{3.5}$$

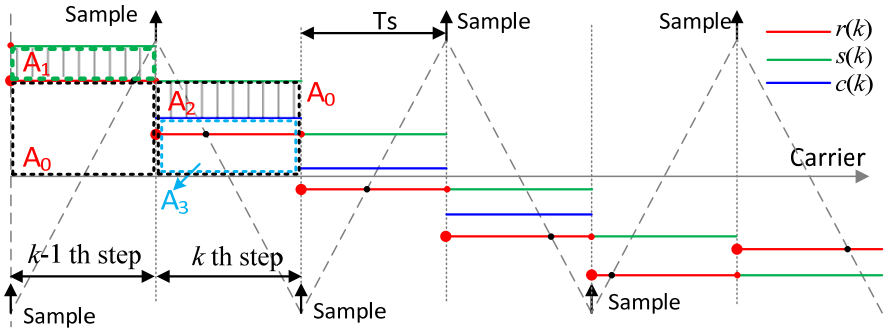

Figure 3-5 The area illustration for the linear predictor [46].

From Figure 3-5, it can be seen that area A_0 is the impulse area generated by $r(k\text{-}1)$ while area A_1 represents the area activated by the difference between $r(k\text{-}2)$ and $r(k\text{-}1)$ [46]. From (3.5), A_2 value is T_d/T_s times of A_1 value, they are equal to each other A_1= A_2 if the delay time T_d=T_s [46]. Therefore, the area A_3 representing the $c(k)$ can be predicted by removing A_2 from A_0, the equivalent phase of the compensated signal is approaching the ideal waveform $r(k)$ [46].

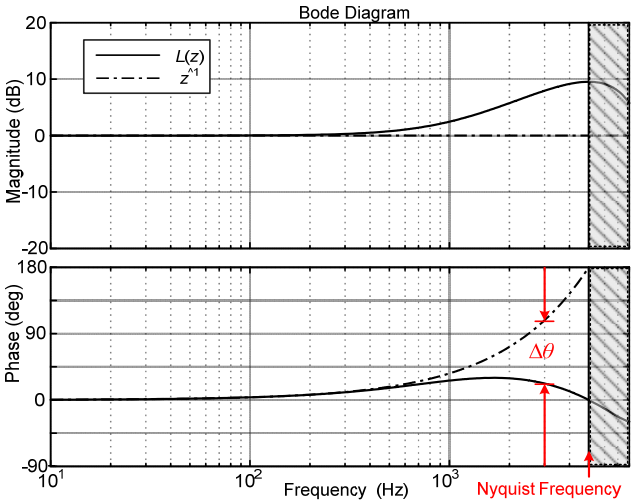

Figure 3-6 Bode diagrams for the linear predictor L(z) and pure phase lead $z^{\wedge 1}$ [46].

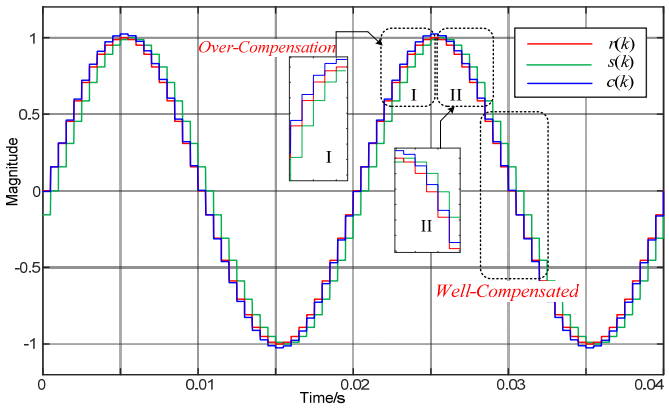

Figure 3-7 Delay compensation results of the linear predictor [46].

Linear predictor operates without system information and predicts the future data just through a linear function [46]. Regrettably, a compulsory requirement is to assure the condition $\omega \cdot T_d$ <0.05 [44], then an accurate linear extrapolation can be guaranteed [46]. Figure 3-6 plots the $L(z)$ Bode diagram supposing the $T_d = T_s$, from

which it can be observed that the phase difference $\Delta\theta$ between the linear predictor and ideal compensation element $z^{\wedge 1}$ increases with the frequency [46]. It means that, in the high frequency range, $L(z)$ actually cannot provide satisfactory compensation.

Figure 3-7 verifies the linear predictor compensation ability by plotting the time-domain result. It can be observed that area A_2 has almost the same area within the zero-crossing vicinity, the delayed signal $s(k)$ almost chases on the ideal signal $r(k)$ [46]. On the other hand, over-compensation, however, happens near the peak parts due to the rapid change of the A_2 [46]. In summary, this scheme, namely linear predictor, cannot well meet the accurate compensation requirement [46].

3.2.2.2 Compensation Scheme based on First-Order-Filter

Besides the linear predictor, a First-Order-Filter (FOF) based method is proposed in [49] to reduce the time delay, and resulting in a widened active damping region [46]. As shown in Figure 3-8, the FOF scheme is configured in a feedback structure whose essence is actually a recursive IIR digital filter [46]. In the figure, the $r(k)$ is the input signal, $c(k)$ is the output signal.

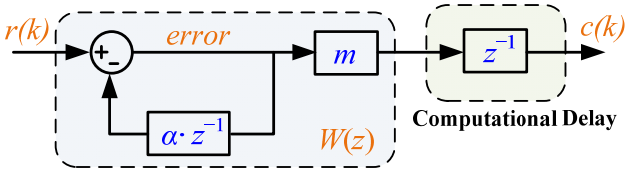

Figure 3-8 Block diagram for the First-Order-Filter compensation method [46].

The discrete transfer function of the compensation method can be written as [46]

$$W(z) = \frac{m}{1+z^{-1}} \Rightarrow \frac{m}{1+\alpha\cdot z^{-1}} \tag{3.6}$$

To guarantee the unity magnitude at the low frequencies, coefficient m is set to $1+\alpha$ because the magnitude of z^{-1} is equal to 1 at such frequencies [46]. (3.7) and (3.8) present the relationship between the output $c(k)$ and input $r(k)$ [46].

$$\frac{c(k)}{r(k)} = \frac{m}{1+\alpha\cdot z^{-1}}\cdot z^{-1} \tag{3.7}$$

$$c(k) = (1+\alpha)\cdot r(k-1) - \alpha\cdot c(k-1) = r(k-1) + \alpha\cdot\{r(k-1) - c(k-1)\} \tag{3.8}$$

(3.8) is still valid if both sides are multiplied by the same variable T_s which is written in (3.9) [46]. Figure 3-9 presents the explanation in detail where the $c(k)$ is

generated by using the (3.9) [46]. A_0 stands for the impulse area generated by $r(k\text{-}1)$ while the area A_1 is the impulse difference activated by the difference between $r(k)$ and $c(k)$ at the $(k\text{-}1)^{th}$ step [46]. Hereby, the impulse area A_3 can be calculated exactly according to equation (3.9).

$$\underbrace{c(k)\cdot T_s}_{A_3} = \underbrace{r(k-1)\cdot T_s}_{A_0} - \overbrace{\alpha\cdot\{c(k-1)-r(k-1)\}\cdot T_s}^{A_2}\underbrace{\qquad}_{A_1} \tag{3.9}$$

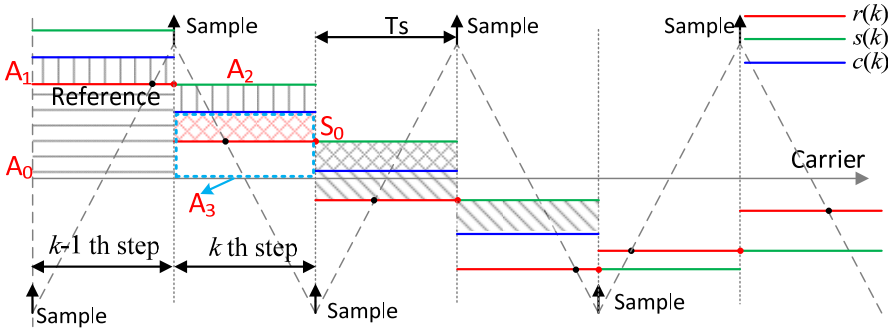

Figure 3-9 The graphical illustration of the FOF based method [46].

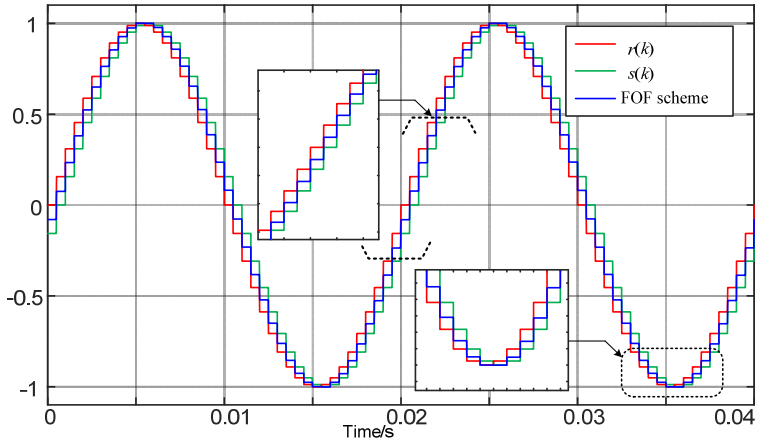

Figure 3-10 Delay compensation result for the FOF compensation method [46].

Figure 3-10 presents the time-domain results for verifying the delay compensation effect where the α and m are selected to 0.95 and 1.95, respectively [46]. The input signal is an ideal fundamental frequency sinusoidal waveform [46]. The sampling frequency is chosen as 2 kHz to assure clear observation on the phase lead feature [46]. It can be seen that the value of the compensated $c(k)$ approximately equals to

the average value of the $r(k)$ and $s(k)$ at every single step [46]. From the compensation results, it provides more accurate phase compensation performance within the peak vicinity than the *Linear predictor* [46].

3.2.2.3 SOGI-based Compensator

In [24], a SOGI-based delay compensator is adopted in the grid current feedback control for the LCL-filtered grid converters [46]. Fundamentally, as shown in Figure 3-11, this method uses the phase lead feature of the second-order resonant term [46]. This figure compares the Bode diagram of the ideal cases with $\omega_c = 0$ rad/s and non-ideal case $\omega_c = 3140$ rad/s [46]. The transfer function of the SOGI-based method is written as

$$E(s) = 1 + \frac{k \cdot \omega' \cdot s}{s^2 + \omega'^2} \Rightarrow 1 + \frac{k \cdot \omega' \cdot s}{s^2 + \omega_c \cdot s + \omega'^2} \tag{3.10}$$

where ω' is the natural frequency, $\omega_c \cdot s$ is the damping term and k is a constant [46].

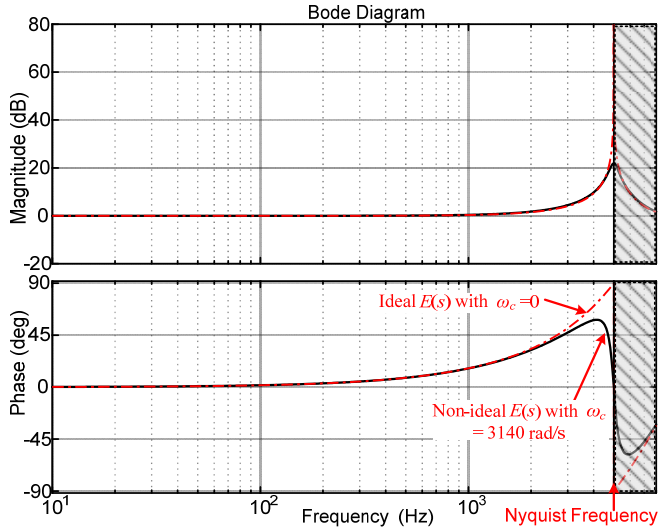

Figure 3-11 Bode diagrams of the SOGI-based compensation scheme [46].

The equation (3.10) can be transferred to form as (3.11) where second order element z^{-2} is introduced [46]. The parameters a, b, c, d, e are constants changing with the ω_c, of which the constant c is a small value (c <0.1) when the ω_c ranges from 0 to 10000 rad/s [46]. In order to guarantee the unit magnitude at the low frequency range, these constants are restricted by the requirement in (3.12) [46].

$$E(z)=\frac{a+b\cdot z^{-1}+c\cdot z^{-2}}{1+d\cdot z^{-1}+e\cdot z^{-2}} \tag{3.11}$$

$$a+b+c=1+d+e \tag{3.12}$$

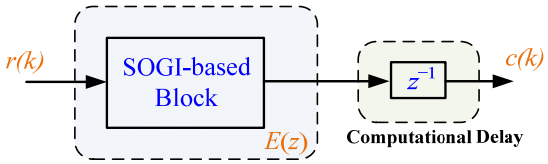

Figure 3-12 Block diagram of SOGI-based compensation scheme [46].

For better illustrating the compensation ability, the case $\omega_c = 0$ as shown in Figure 3-11, k equals to 1.414 is studied [46]. Similar with the illustration in the previous subsection, equation (3.13) writes the transfer function and Figure 3-13 presents the graphical illustration, where area A_0, A_1, A_2, A_3 are marked, and the $c(k)$ is predicted according to (3.14) [46].

$$E(z)=\frac{1.9+2\cdot z^{-1}+0.1\cdot z^{-2}}{1+2\cdot z^{-1}+z^{-2}}=\frac{1.9+0.1\cdot z^{-1}}{1+z^{-1}} \tag{3.13}$$

$$\underbrace{c(k)\cdot T_s}_{A_3}=\underbrace{r(k-1)\cdot T_s}_{A_0}-0.9\cdot\underbrace{\{c(k-1)-r(k-1)\}\cdot T_s}_{A_1}+0.1\cdot\underbrace{\{r(k-2)-c(k-1)\}\cdot T_s}_{A_2} \tag{3.14}$$

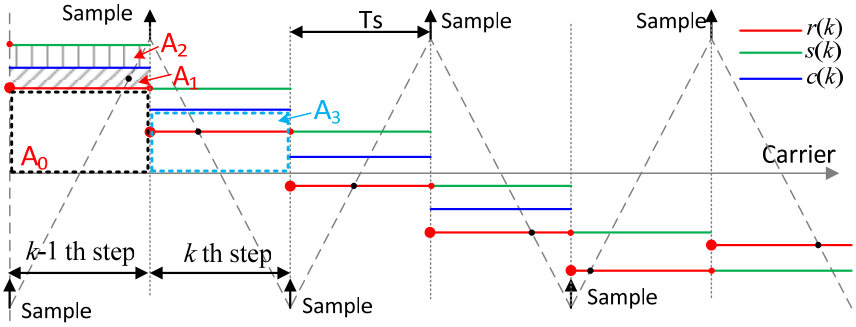

Figure 3-13 The graphical representation of the SOGI-based compensation scheme [46].

From equation (3.6), the SOGI-based scheme actually owns similar form with the FOF based scheme except the term $0.1\cdot z^{-1}$ [46]. Regrettably, this term make the compensation ability poorer which is in agreement with the analysis [46]. Figure 3-14 presents its compensation result and it shows quite similar compensation ability with the FOF based scheme [46].

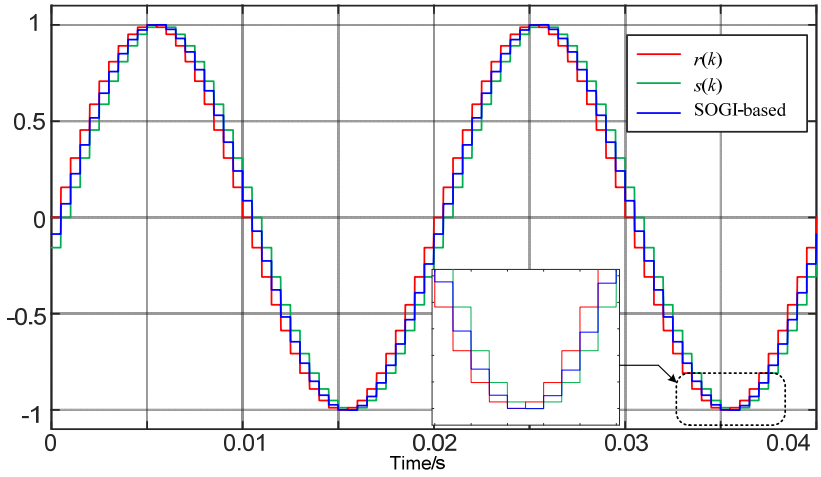

Figure 3-14 Delay compensation result for the SOGI-based compensation scheme [46].

3.3. AN IMPROVED COMPENSATION SCHEME [46]

3.3.1. PRINCIPLE

This section proposes an improved delay compensation method based on the graphical explanation of FOF and SOGI-based schemes [46]. Based on (3.9) and Figure 3-9, the signal after compensation can further approach the ideal signal and then the equivalent phase is also closer to the ideal signal [46]. As shown in Figure 3-15(a), this goal could be ideally achieved through mathematically removing the area S_0, which is expressed as

$$S_0 = \{c(k) - r(k)\} \cdot T_s \;\Rightarrow\; S_1 = \{c(k-1) - r(k-1)\} \cdot T_s \tag{3.15}$$

where S_0 represents the area difference between $c(k)$ and $r(k)$ [46]. If S_0 could be fully compensated, then the time delay would be totally canceled. Regrettably, both signals are the ones at current step to be calculated, therefore, such a mathematical removal is not practical in a digital controller [46]. To replace the area S_0, area S_1 can be used, whose expression is also written in (3.15), however, this substitution will bring an unstable pole, which is presented and derived in [46]. In Figure 3-15(b), this thesis proposes a feasible S_0 alternative: Some proportion of area S_2, notated as area A_4 and expressed in (3.16).

$$A_4 = \beta \cdot S_2 = \beta \cdot \{r(k-2) - r(k-1)\} \cdot T_s \tag{3.16}$$

where β is the proportion factor [46]. The expression after inserting compensation block can be presented as

$$\underbrace{c(k)\cdot T_s}_{A_3} = \underbrace{r(k-1)\cdot T_s}_{A_0} - \overbrace{\alpha\cdot\{c(k-1)-r(k-1)\}\cdot T_s}^{A_2} - \overbrace{\beta\cdot\{r(k-2)-r(k-1)\}\cdot T_s}^{A_4} \tag{3.17}$$

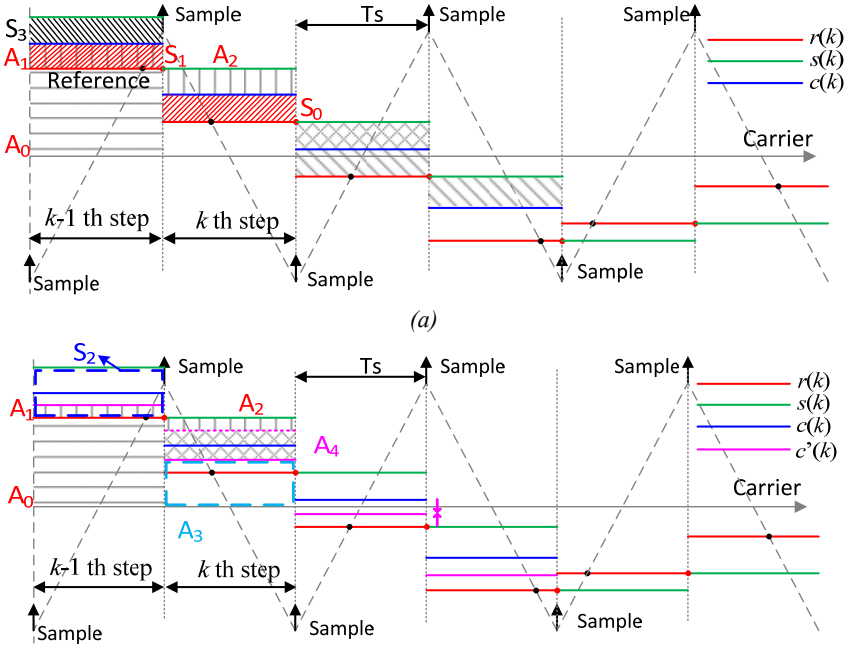

Figure 3-15 The graphical illustration of the proposed compensation scheme: (a) the expression of area difference S_0, (b) area termA_4 to replace S_0 [46].

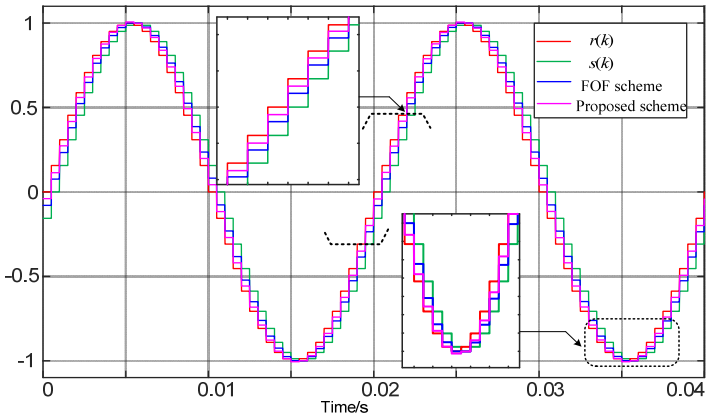

Figure 3-16 Delay compensation result for the proposed compensation scheme [46].

Same with other methods, Figure 3-15(b) presents the graphical explanation of the proposed scheme: the signal $c(k)$ represents the conventional FOF based compensation whereas the $c'(k)$ is the signal after inserting an additional area A_4 [46]. In comparison to the phase of signal $c(k)$, the equivalent phase of $c'(k)$ is closer to the $r(k)$, demonstrating the compensation effects of the proposed method [46].

Figure 3-16 presents the time-domain results while this proposal is adopted, where the FOF based scheme and proposed scheme are compared. As stated earlier, the FOF based scheme can compensate the delayed signal to the middle of the signal $r(k)$ and $s(k)$. By comparison, the proposed scheme can even compensate about one quarter more than the FOF based scheme.

3.3.2. PROPOSAL FORMATION

In order to realize the proposal in a real micro-processor, the data in the previous steps, which is stored in the buffer register, is required for future data prediction [46]. For instance, the data at $(k\text{-}1)^{th}$ step, such as $r(k\text{-}1)$ and $c(k\text{-}1)$ along with the data at $(k\text{-}2)^{th}$ step $r(k\text{-}2)$ are available for the prediction of the k^{th} step $c(k)$ [46]. According to equation (3.17), the discrete transfer function can be expressed as [46]

$$\frac{c(k)}{r(k)} = \frac{(1+\alpha+\beta)-\beta\cdot z^{-1}}{1+\alpha\cdot z^{-1}}\cdot z^{-1} \tag{3.18}$$

$$H^*(z) = \frac{(1+\alpha+\beta)-\beta\cdot z^{-1}}{1+\alpha\cdot z^{-1}} \tag{3.19}$$

According to the transfer function in (3.19), the block diagram of the proposed method is shown in Figure 3-17, where the coefficient n is equal to $1+\alpha+\beta$ [46].

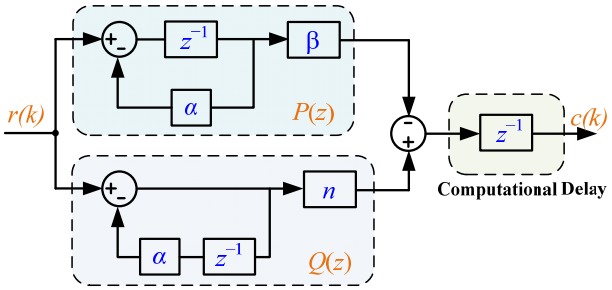

Figure 3-17 Structure of the proposed compensation method [46].

3.3.3. IMPACT OF COEFFICIENT TUNING

For a particular case, if $\beta = 0$, the proposed method turns into the FOF based method,

the basic compensation reasoning is that the introduction of β changes the phase-lead feature of the proposed compensation block. Its value decides the phase-lead extent of the proposed scheme: A larger β generates a better compensation result, however, a large magnitude also appears near the Nyquist frequency as shown in Figure 3-18, reducing its immunity to noise [46]. On the other hand, a smaller β cannot have satisfactory compensation effects. Figure 3-18 presents the Bode diagrams with β varying from 0 to 2 [46].

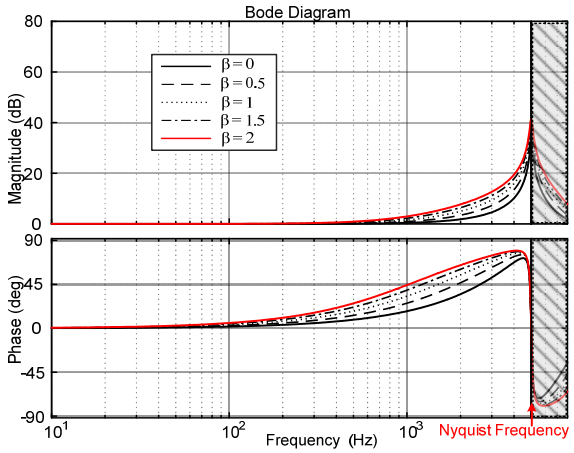

Figure 3-18 Bode diagrams with different β values [46].

3.3.4. COMPARISON RESULTS

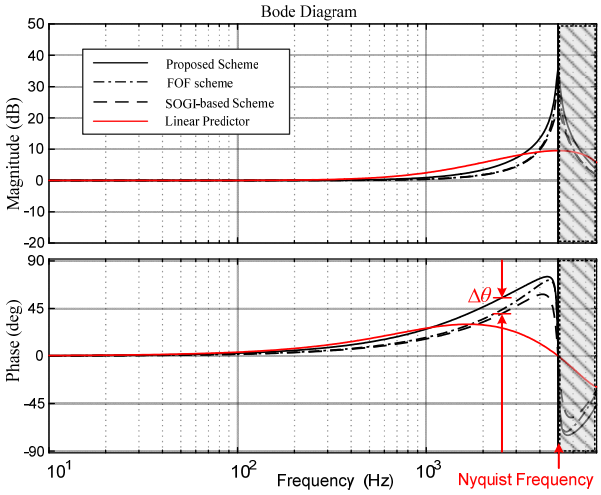

Figure 3-19 Bode diagram comparison of four different compensation schemes [46].

To comprehensively these four compensation schemes, Figure 3-19 presents the frequency responses of different compensation methods studied in past parts. The parameters can be found in [46]. From the figure, all these four compensation methods have phase lead effect, then time delay can be compensated [46]. Among these four methods, the proposed scheme has the best compensation result, the second one is the FOF method, next is the SOGI-based method while the linear predictor has the worst compensation effect [46].

3.4. VERIFICATION FOR THE PROPOSAL

3.4.1. MODELING AND ANALYSIS

To verify the effectiveness of the proposed method, a grid-connected inverter with an output LCL filter is employed whose topology is given in Figure 3-20, L_1 is the inverter-side inductor, C is the filter capacitor and L_2 is the grid-side inductor [46]. In order to guarantee the current quality, the inverter-side current i_1 is controlled, the PCC voltage is used for grid synchronization [46].

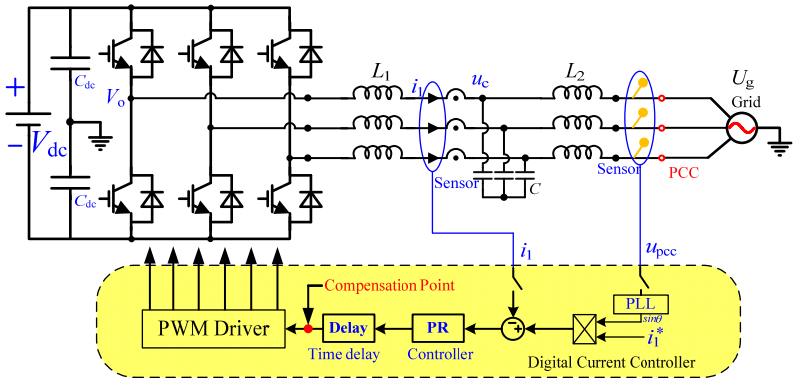

Figure 3-20 Topology and control of LCL-filtered grid-connected inverter [46].

The system plant can be obtained where the function $G_{i1}(s)$ for relating the converter output voltage to the inverter-side current i_1 can be derived as:

$$G_{i1}(s) = \frac{i_1(s)}{V_0(s)} = \frac{s^2 L_2 C + 1}{s^3 L_1 L_2 C + sL_1 + sL_2} \tag{3.20}$$

As demonstrated in [25], the current loop is always stable regardless of the LCL filter and controller parameters if the delay is not considered [46]. So it is a straightforward way to stabilize such a system through decreasing the digital delay [46]. The inverter parameters can be found in [46]. Figure 3-21 plots the root loci for the studied compensation schemes, where it can be observed that, if no compensation method is inserted, the system is always unstable because two system

poles are always out of the unit circle [46]. In agreement with the previous analysis, the proposed method can provide best compensation effect among these compensation schemes [46].

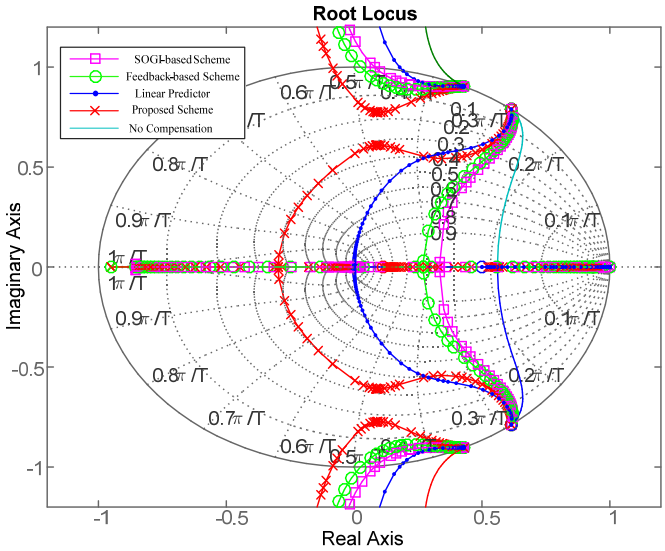

Figure 3-21 Root loci for different delay compensation schemes [46].

3.4.2. SIMULATION RESULTS

Figure 3-22 and 3-23 show the time-domain simulation results using the same parameter with previous part, the inductor equivalent series resistors are chosen as 0.2Ω in the simulation model to emulate the inverter system [46]. Figure 3-22 (a) and (b) present the dynamic responses for the grid current with applications of the linear predictor and SOGI-based method, respectively [46]. The transient behaviors for the reference from 10 A to 5A can be observed and compared.

In Figure 3-22 (a), the current shows obvious oscillations, meaning that the system phase margin is relatively small [46]. Figure 3-22 (b) shows the simulation results where the SOGI-based method is adopted, from which the dynamic response becomes better with shorter settling time [46]. This improvement indicates that the current control loop bandwidth has been broadened through reducing the time delay [46]. Figure 3-23 (a) and (b) replace the compensation method with the FOF method and the proposed scheme, the same operating conditions and the same control parameters are applied [46]. Compared with results in Figure 3-22, the proposed scheme exhibits significant dynamic improvement, the settling time is much shorter than the linear predictor, FOF method and SOGI-based method [46].

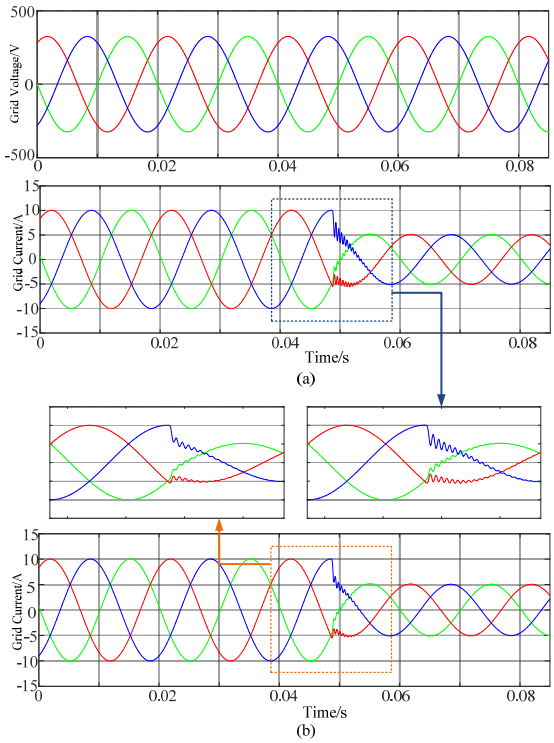

Figure 3-22 Simulation results (a) Linear predictor, (b) SOGI-based scheme [46].

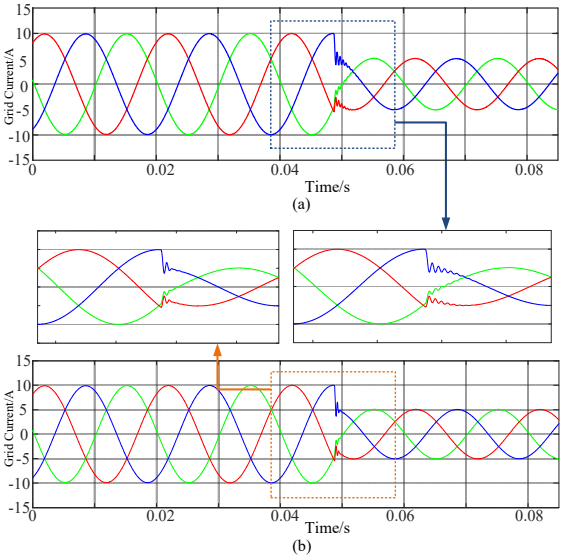

Figure 3-23 Simulation results (a) FOF scheme; (b) Proposed scheme [46].

3.4.3. EXPERIMENTAL RESULTS

The experiments are executed in a lab-scale prototype. The description of these experiments conditions are illustrated in the paper [46]. In the experiments, the external conditions should be the identical for different compensation methods, including the same control parameters, LCL filter and operating conditions [46]. Figure 3-24 to 3-27 show the delay compensation effects while applying four different compensation methods.

Summarizing these experimental results and the comparison results are presented: At first, in Figure 3-24, the linear predictor exhibits more than 10 settling cycles, then Figure 3-25 presents the transient behavior of the SOGI-based scheme, in comparison with linear predictor, it has about 5 settling cycle [46]. Similarly, the FOF method also has about 5 settling cycles in Figure 3-26 [46]. Better than last three methods, the proposed scheme exhibits the best dynamic performance, it only has one settling cycle [46]. The experimental results are in good agreement with the simulations and the analysis results.

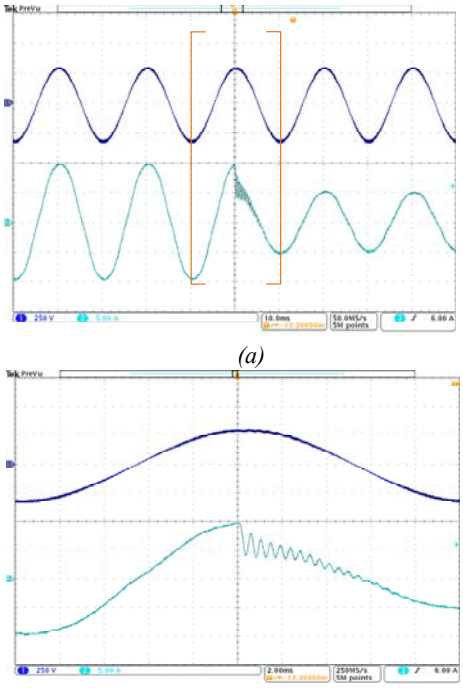

(a)

(b)

Figure 3-24 Dynamic response with the Linear predictor: (a)10 A to 5 A (b) Zoom in[46].

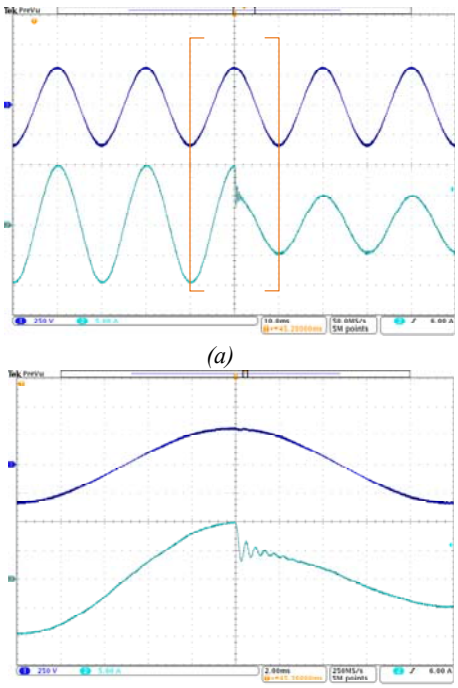

(a)

(b)

Figure 3-25 Dynamic response with SOGI-based scheme: (a)10 A to 5 A (b) Zoom in[46].

3.5. CONCLUSION

The chapter focuses on the graphical illustration of several compensation schemes for the intrinsic time delays in the digital processor. Using a unified explanation and evaluation method, the essential reason of different compensation methods is clearly revealed [46]. Moreover, based on the evaluation, a practical and straightforward compensation method with superior compensation result is then proposed in this chapter [46]. Compared to the existing compensation strategies, the proposed compensation method is demonstrated to be a promising alternative to replace the conventional ones [46]. Finally, an application example, a LCL-filtered inverter, is tested to verify the theoretical analysis and the experimental results comparing the transient behaviors verify the effectiveness of the proposed scheme [46].

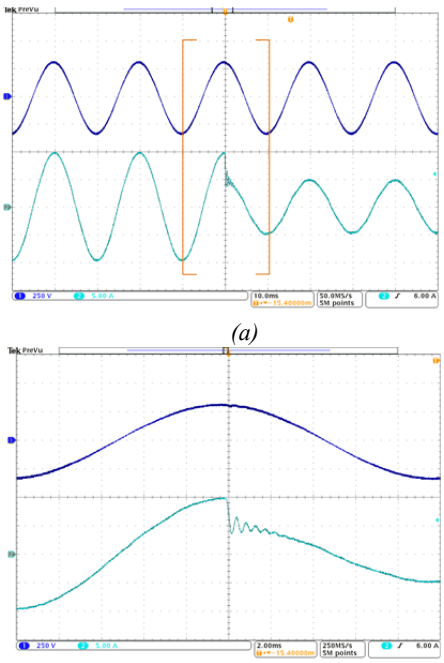

(a)

(b)

Figure 3-26 Dynamic response with the FOF scheme: (a)10 A to 5 A (b) Zoom in [46].

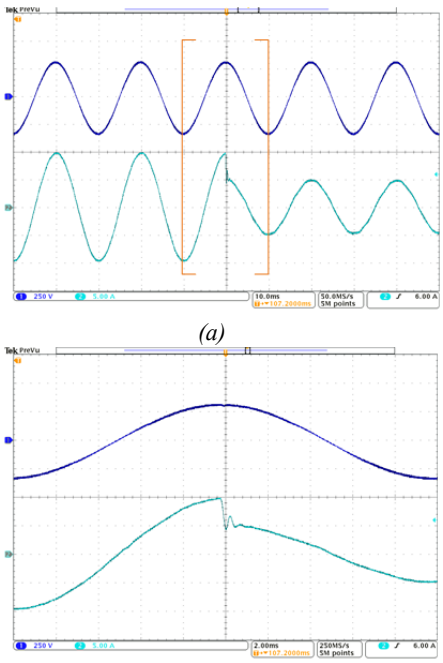

(a)

(b)

Figure 3-27 Dynamic response with proposed scheme: (a)10 A to 5A (b) Zoom in [46].

CHAPTER 4. RESONANCE INTERACTION OF LCL-FILTERED GRID-CONNECTED INVERTERS [20]

In this chapter, system resonance and stability issue of multi-parallel grid-connected inverters with LCL-filter have been studied. The analysis reveals that multiple resonances at different frequencies could be excited in such a system, which is different from the situation with single inverter [20]. A separate current modeling scheme is presented in this study. It reveals that resonance may not only happen in the grid injecting current, but also the interactive current circulating between the paralleled inverters [20]. Different from the grid current resonance, this phenomenon has yet been discussed before, the stability analyses of these two currents are carried out in the discrete domain with two different stability constraints identified [20].

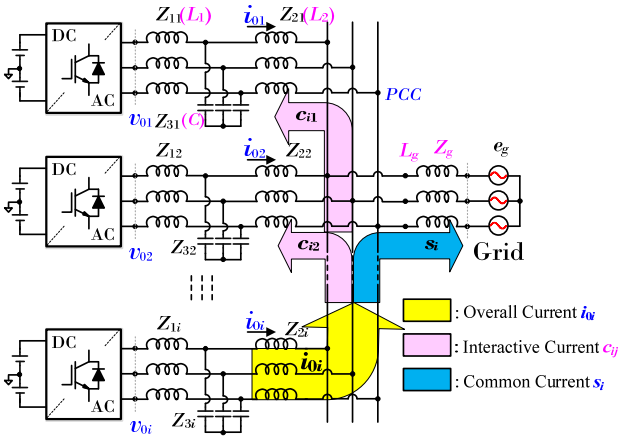

Figure 4-1 Parallel operation of multiple grid-connected inverters with LCL-filter [20].

4.1. MODELING OF PARALLEL-CONNECTED INVERTERS

4.1.1. MODELING

In Figure 4-1, the parallel operation of multiple grid-connected inverters with LCL-filter is presented, Z_{1i} and Z_{2i} (i=1$\cdots n$) are converter-side and grid-side impedances, Z_{3i} are the capacitor impedances, Z_g is the grid impedance for the weak power system [20]. v_{0i} are the inverter output voltages, i_{0i} are the grid currents injecting to the grid and e_g is the ideal grid voltage [20].

The dynamics of the multi-paralleled inverters system can be described with multivariable system theory in which each inverter output voltage v_{0i}represents an input and each inverter current i_{2i} represents output to the multi-inverters system [12]. The expression between the grid current i_{0i} and voltage v_{0j} can be written as

$$\begin{aligned}&\mathbf{I}(\mathrm{s})=\boldsymbol{G}(\mathrm{s})\cdot\mathbf{U}(\mathrm{s})\Leftrightarrow\\&\begin{pmatrix}i_{01}\\i_{02}\\\cdots\\i_{0n}\end{pmatrix}=\boldsymbol{G}(\mathrm{s})\cdot\begin{pmatrix}v_{01}\\v_{02}\\\cdots\\v_{0n}\end{pmatrix}=\begin{pmatrix}G_{11}&G_{12}&\cdots&G_{1n}\\G_{21}&G_{22}&\cdots&G_{2n}\\\cdots&\cdots&\cdots&\cdots\\G_{n1}&G_{n2}&\cdots&G_{nn}\end{pmatrix}\cdot\begin{pmatrix}v_{01}\\v_{02}\\\cdots\\v_{0n}\end{pmatrix}\end{aligned}\tag{4.1}$$

where $\boldsymbol{G}$(s) is transfer function matrix, describing the relationship of each v_{0i} and the i_{0j}, for example, G_{11} means the impact of v_{01} on the self-current i_{01}, and G_{12} means the impact of v_{02} on the current i_{01} [20]. **I**(s) and **U**(s) represent the current and voltage vectors, respectively. In this study, these inverters are supposed to be of the same product type with small parameters mismatch, hence, the diagonal elements are equal since each v_{0i} has identical impact on its own currenti_{0i}, i.e. G_{ii} =G_{11} [20]. Similarly, all non-diagonal elements are also identical since v_{0i} has the identical influence on other i_{0j}, i.e. G_{ij} =G_{12} ($i\neq j$), $\boldsymbol{G}$(s) possesses the symmetry characteristic [20]. The elements G_{11} and G_{12} are obtained using the principle of linear superposition, similar derivation method with [58], the expressions are shown in (4.2) [20].

$$\begin{cases}G_{11}=\dfrac{n-1}{n}\cdot G_{plant}+\dfrac{1}{n}\cdot G_{coupling}\\G_{12}=-\dfrac{1}{n}\cdot G_{plant}+\dfrac{1}{n}\cdot G_{coupling}\end{cases}\tag{4.2}$$

where G_{plant} and $G_{coupling}$ are written as [20]

$$\begin{aligned}G_{plant}(s)&=\frac{Z_3}{Z_1Z_2+Z_2Z_3+Z_3Z_1}=\frac{1}{sL_1L_2C}\cdot\frac{1}{(s^2+w_{res}^2)}\\G_{coupling}(s)&=\frac{1}{sL_1(L_2+nL_g)C}\cdot\frac{1}{(s^2+w_{res1}^2)}\end{aligned}\tag{4.3}$$

where ω_{res}=$\sqrt{(L_1+L_2)/L_1L_2C_f}$;$\omega_{res1}$= $\sqrt{(L_1+L_2+nL_g)/L_1(L_2+nL_g)C_f}$.

From (4.2), it can be seen that the non-diagonal element G_{12} is equal to zero if the grid impedance Z_g =0 for the ideally stiff grid. It means that there is no mutual coupling among these inverters, which operate just as a single one, these inverters cannot be seen by each other, all the inverters currents flow directly to the power grid [20]. Comparatively, for the weak grid case, these parallel-connected inverters are coupled due to the grid impedance Z_g and influence each other as a result [20].

For the *i*# converter, as shown in Figure 4-1, the grid current i_{0i} can be divided into *n* parts: *n*-1 parts to the other inverters and one part to the power grid, and can be written as (4.4) [20].

$$\boldsymbol{i}_{0i} = \boldsymbol{c}_{i1} + \boldsymbol{c}_{i2} + \ldots + \boldsymbol{c}_{in} + \boldsymbol{s}_i = \sum \boldsymbol{c}_{ij} + \boldsymbol{s}_i = \boldsymbol{c}_i + \boldsymbol{s}_i \tag{4.4}$$

where c_{ij} is the current circulating from the *i*# to the *j*# inverter and is named as the *interactive current*; on the other hand, s_i is the current to the power grid, named as the *common current* [20]. Figure 4-1 plots the current distribution of the whole system, where the interactive current c_{ij} and the common current s_i are illustrated [20]. According to (4.1) and (4.2), the whole current vector **I**(s) can be obtained as [73]

$$\mathbf{I}(\mathrm{s}) = (\mathrm{A}_1(\mathrm{s}) + \mathrm{A}_2(\mathrm{s})) \cdot \mathbf{U}(\mathrm{s}) \tag{4.5}$$

where $\mathbf{A_1}$(s) and $\mathbf{A_2}$(s) can be written as

$$\mathrm{A}_1(\mathrm{s}) = \boldsymbol{G}_{plant}(\boldsymbol{s}) \cdot \begin{pmatrix} (n-1)/n & -1/n & \cdots & -1/n \\ -1/n & (n-1)/n & \cdots & -1/n \\ \cdots & \cdots & \cdots & \cdots \\ -1/n & -1/n & \cdots & (n-1)/n \end{pmatrix} \tag{4.6}$$

$$\mathrm{A}_2(\mathrm{s}) = \boldsymbol{G}_{coupling}(\boldsymbol{s}) \cdot \begin{pmatrix} 1/n & 1/n & \cdots & 1/n \\ 1/n & 1/n & \cdots & 1/n \\ \cdots & \cdots & \cdots & \cdots \\ 1/n & 1/n & \cdots & 1/n \end{pmatrix} \tag{4.7}$$

The interactive current and common current model can be expressed as [20]

$$\mathbf{C}(\mathrm{s}) = \mathrm{A}_1(\mathrm{s}) \cdot \mathbf{U}(\mathrm{s}),\ \mathrm{S}(\mathrm{s}) = \mathrm{A}_2(\mathrm{s}) \cdot \mathbf{U}(\mathrm{s}) \tag{4.8}$$

where $\mathbf{C}(\mathrm{s})=[c_1, c_2, \cdots, c_n]^{\mathrm{T}}$, $\mathbf{S}(\mathrm{s})=[s_1, s_2, \cdots, s_n]^{\mathrm{T}}$, therefore, i_{0i}(*i*=1 for instance) is expressed as [20]

$$\begin{aligned} \boldsymbol{i}_{01} &= \boldsymbol{G}_{11} \cdot \boldsymbol{v}_{01} + \sum_{k=2}^{n} \boldsymbol{G}_{12} \cdot \boldsymbol{v}_{0k} \\ &= \frac{1}{\boldsymbol{n}} \boldsymbol{G}_{plant} (\underbrace{\boldsymbol{v}_{01} - \boldsymbol{v}_{02}) + \cdots + \frac{1}{\boldsymbol{n}} \boldsymbol{G}_{plant} (\boldsymbol{v}_{01} - \boldsymbol{v}_{0n}}_{\text{Interactive Current (n-1) terms } \boldsymbol{c_i}}) + \frac{1}{\boldsymbol{n}} \underbrace{\boldsymbol{G}_{coupling} (\boldsymbol{v}_{01} + \cdots + \boldsymbol{v}_{0n})}_{\text{Common Current } \boldsymbol{s_i}} \end{aligned} \tag{4.9}$$

4.1.2. MULTIPLE RESONANCE CHARACTERISTIC [20]

From the equation (4.9), the dynamics of the interactive currents are only decided by G_{plant} while the common current is only dependent on the $G_{coupling}$ only, hence, the dynamics can be analyzed by two independent transfer functions G_{plant} and $G_{coupling}$ if the power system is weak [20]. Note that G_{plant} neither depends on the number of inverters N nor on the grid impedance Z_g, thus, the c_{ij} dynamic is the same whether in a plant there are few or many inverters, or whether the grid is strong or weak, whereas the s_i dynamic is completely different [20]. Both the G_{plant} and $G_{coupling}$ have their individual resonance peak as presented in Figure 4-2, where two resonance peaks exist at ω_{res} and ω_{res1}, respectively, they are the interactive current resonance and common current resonance as shown in the figure [20].

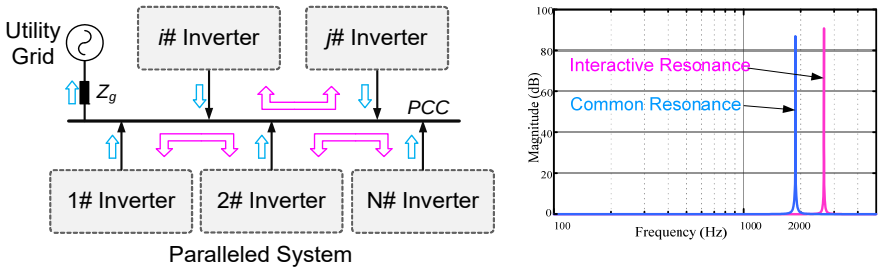

Figure 4-2 Interactive current and common current and resonance characteristic [20].

4.2. CONTROL SCHEME AND STABILITY ANALYSIS

4.2.1. CONTROL SCHEME

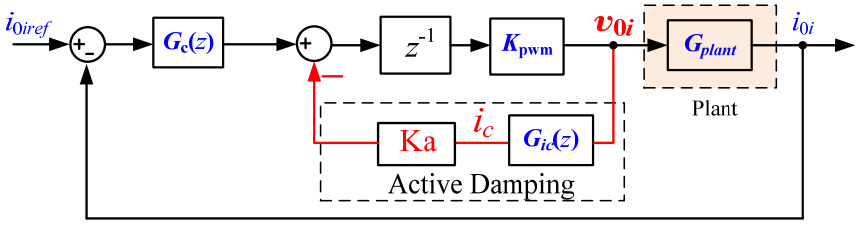

Figure 4-3 Control block diagram in the z-domain [20].

As mentioned earlier, these paralleled grid-connected inverters are coupled to each other due to the grid impedance in the weak power grid, regrettably, because each converter module has its individual controller without communication cable, in such a decentralized controller, it is not easy to adopt control scheme to decouple these inverter [20]. For every single inverter, Figure 4-3 shows the grid-side current i_{0i} control block diagram, in which the inverter bridge is regarded as gain K_{pwm}, the G_c

and G_{plant} are the transfer functions of the controller and LCL-filter plant, respectively [20]. In this study, the filter capacitor current feedback active damping is used, G_{ic} is the transfer function between the capacitor current and inverter output voltage. K_a is the damping coefficient, moreover, the analysis is performed in z-domain. The digital one-sample delay z^{-1} is considered [20].

4.2.2. ROOT LOCUS ANALYSIS FOR STABILITY

From the current separation analysis, the interactive current c_{ij} and common current s_i have different plants G_{plant} and $G_{coupling}$, respectively [20]. It means that it is able to analyze two currents stability separately, therefore, the stability analysis can be divided into *interactive current stability* and *common current stability* [20]. In (4.10), $T_p(z)$ is the open-loop transfer function for interactive current, where $D(z)$ the active damping part in Figure 4-3 and $G_{plant}(z)$ is the interactive current plant transfer function in the z-domain [20]. $T_u(z)$ is the open-loop transfer function for common current, $G_{coupling}(z)$ is the common current plant transfer function in the z-domain [20].

$$\begin{aligned} T_p(z) &= G_c(z) \cdot D(z) \cdot G_{plant}(z) \\ T_u(z) &= G_c(z) \cdot D(z) \cdot G_{coupling}(z) \end{aligned} \tag{4.10}$$

where $D(z)= z^{-1}K_{pwm}/(1+ z^{-1}K_{pwm}KG_{ic}(z))$.

The multi-inverters system is stable if and only if the two stability requirements are satisfied at the same time, namely the close loop poles of $T_p(z)$ and $T_u(z)$ are located inside the unit circle [20]. Figure 4-4 shows the close-loop poles movement with gain variation for $T_p(z)$ and $T_u(z)$, with different filter and control parameters given in Table I [20]. It can be observed that these two current components have totally different root locus and stable regions, Figure 4-4 (a) plots such two root loci whose parameters can be found in [20], one is for interactive current and the other one is for common current.

Moreover, Figure 4-4 (b) presents a case with the parameter Set II that the common current poles are inside the unit circle while the interactive current poles are outside of the unit circle, it indicates the common current is stable while the interactive current is unstable [20]. Same with parameter Set III, the interactive current is stable whereas the common current is unstable, as shown in Figure 4-4(c) [20].

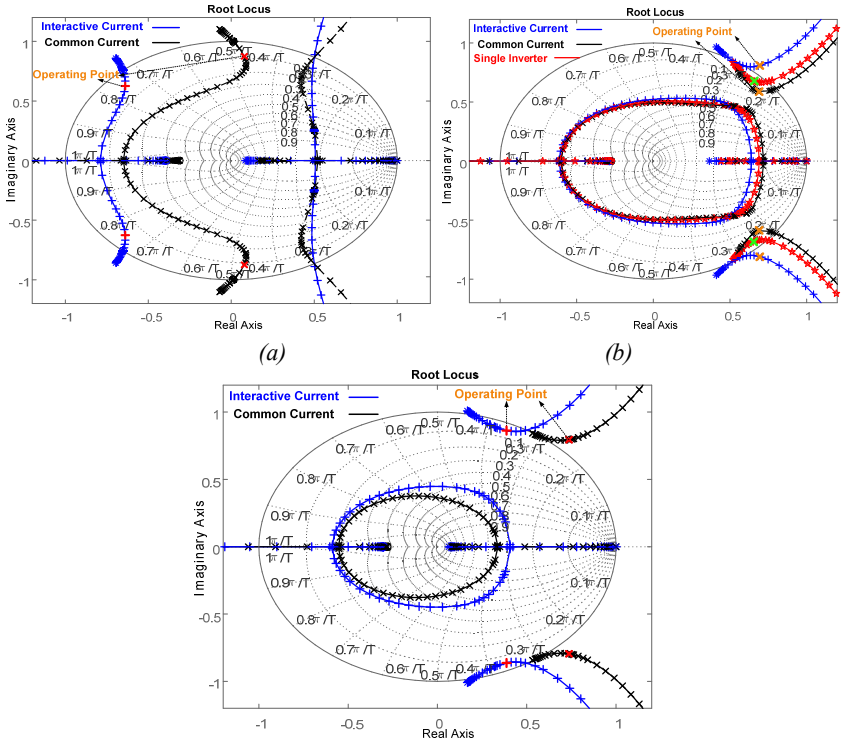

Figure 4-4 System root loci with different filter and control parameters: (a) Interactively stable and commonly stable; (b) Interactively unstable and commonly stable;(c) Interactively stable and commonly unstable [20].

4.3. SIMULATION RESULTS

In this study, the simulations are done by using the Matlab/Simulink, N=2 inverters are considered [20]. At first, the LCL-filter and control parameters of the Set I case in [20] are selected. In agreement with the analysis, the whole system is stable because both interactive current and common current are stable as presented in Figure 4-5: at time t=0.145s, the 1# inverter keeps the same while the current reference jumps from 10A to 15A for 2 # inverter [20]. It can be observed that the paralleled system is stable.

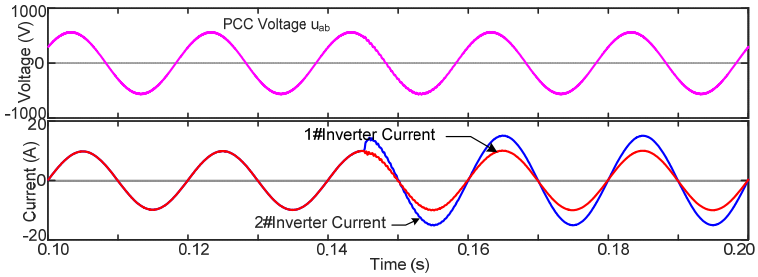

Figure 4-5 Simulation waveforms with Set I LCL filter as selected in [20].

Then the filter and control parameters in Set II are selected for verifying the case of the interactive current instability, Figure 4-4 (b) plot the system poles movement, which can identify system stability [20]. In the figure, the red-marked root locus is for the single inverter in the weak grid case, the operating points are in the unit circle, meaning the single inverter operates stable with such parameters [20]. If the second inverter is inserted in parallel operation, from the root loci, it can be observed that the two-inverter system is commonly stable, meaning the sum of two inverter grid current is stable [20]. However, the poles representing the interactive current are outside the unit circle, meaning that resonant current will circulate between these two inverters, the simulation waveforms are shown in Figure 4-6, where two inverter currents equalize to each other initially [20]. At t=0.145s, the resonant interactive current is triggered, high frequency current circulates between the inverters while the sum current is still stable, in this case, current of each inverter contains two parts: 1) The current injected to the grid at the fundamental frequency, 2) circulating current at filter resonance frequency [20].

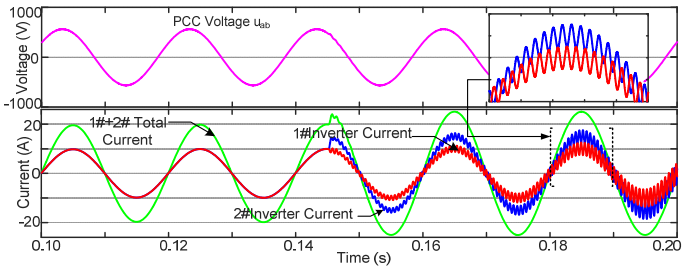

Figure 4-6 Simulation waveforms with Set II LCL-filter (interactively unstable) [20].

Next, Figure 4-4(c) shows the possible case where the two-inverter system is interactively stable, but commonly unstable, with the parameters of Set III, the poles of the interactive current are insides the unit circle, whereas the poles of common current are outsides the unit circle [20]. It explains the case that each inverter module is stable, but the parallel operation makes system unstable when they are connected to the same point in a weak power system, Figure 4-7 shows the simulation waveforms for this case, every current of the inverter module contains

the common current component [20]. Therefore, both two currents contain the resonant currents, the whole paralleled system becomes unstable due to the instability of common current [20].

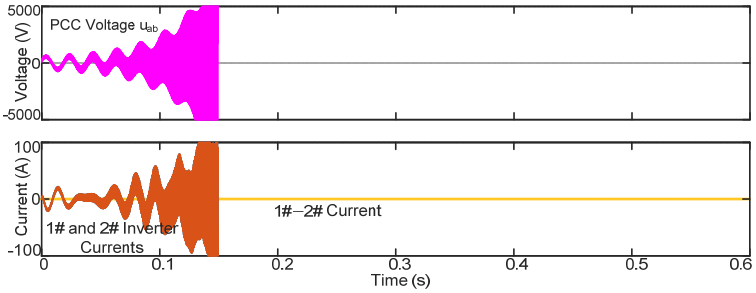

Figure 4-7 Simulation waveforms with Set III LCL filter [20].

4.4. EXPERIMENTAL RESULTS

The experiments are implemented in a two-inverter platform, in which both inverters have identical parameters and are from same manufacturer, the grid in this experiment is built and emulated using a grid simulator rated 15 kW, so the grid impedance can be emulated using an inductor [20]. Corresponding to the simulation results, Figure 4-8 firstly presents the experimental waveforms that the two-inverter system is stable, both for interactive current and common current, obviously, no resonant currents flow in the system if the parameters Set I are selected [20].

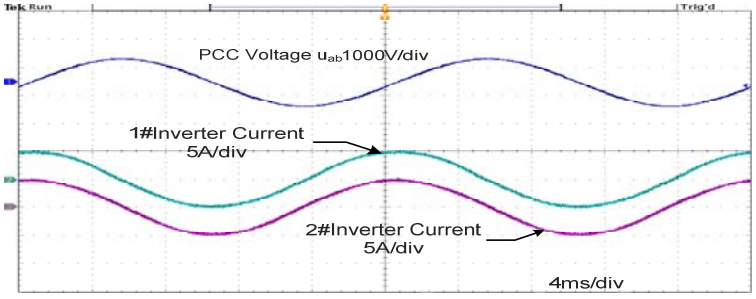

Figure 4-8 Experimental results: both interactively and commonly stable [20].

In the Figure 4-9, the resonant phenomenon verifies the analysis that the interactive current is unstable whereas the sum of the inverter currents is stable, it can be seen the sum of two currents is still sinusoidal, and individual current is resonant [20]. In fact, the resonant current component circulates from the first inverter to the other inverter, vice versa [20]. Because of the stable total current, the voltage at PCC is also sinusoidal, the experimental results are in good agreement with the poles movement analysis in Figure 4-4 (b) [20].

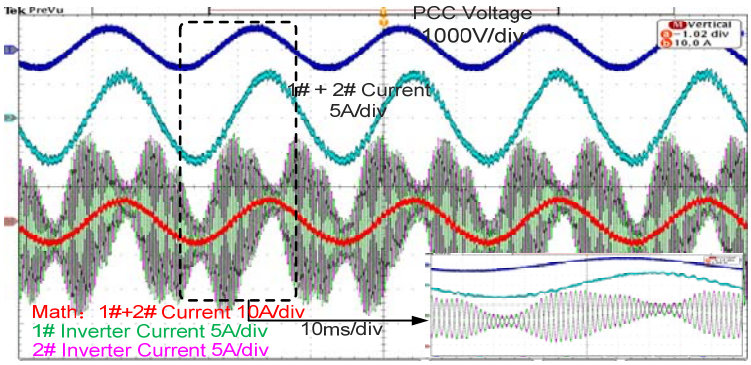

Figure 4-9 Interactive current circulating between inverters [20].

The parameters in Set III are chosen for verifying the common current instability, the experimental results for the unstable case with unstable common currents are shown in the Figure 4-10 [20]. In the figure, any inverter in the system has an unstable dynamic. Also, the currents injected to the power grid are also unstable. This result is also in agreement with the previous root locus plot analysis [20].

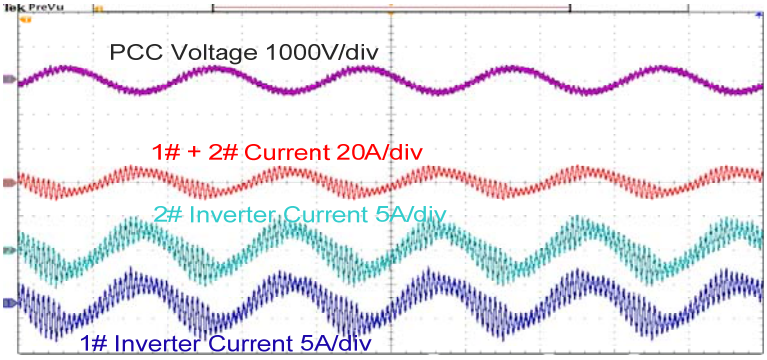

Figure 4-10 Experimental result of commonly unstable [20].

4.5. SUMMARY

This chapter deals with the modeling and stability analysis for the system consisting of multiple grid-connected inverters with LCL-filter. Through dividing the inverter output current into two separate currents: interactive current and common current, the stability of paralleled system can be analyzed through the stability of two currents [20]. The resonant phenomenon that interactive resonant current circulates between two paralleled inverters is first revealed in this paper [20]. Two stability regions are then identified using the root loci plot and analysis in the *z*-domain. Simulation and experimental results verify all the analysis in the paper.

CHAPTER 5. CONCLUSIONS AND FUTURE PERSPECTIVES

This chapter summarizes the research work, which has been presented throughout this thesis, and highlights the main achievement and contributions of this Ph.D. project. Then, this chapter ends up with the future perspectives of this project in order to inspire the future achievement.

5.1. SUMMARY

This thesis mainly focuses on the research subjects: a) stability analysis and region identification of grid-connected inverters for renewable energy generation system, b) digital delays compensation schemes for the digitally-controlled inverters. The first topic has been presented in *Chapter 2* and *Chapter 4*, including the stability analysis of single inverter with *Grid Voltage Feedforward Regulator* (GVFR) and the system with multiple grid-connected inverters with LCL-filter. The second topic is described in *Chapter 3*, where various digital delays compensation schemes are evaluated and compared, moreover, an improved compensation method is proposed.

In the *Introduction* part, the background and motivation of this project has been presented, along with the state of art of the selected topics. The stable and safe operations of power-electronics based power system are gaining increasing research attention. In this context, the studied three topics are introduced.

Chapter 2 has comprehensively discussed the stability issue of grid-connected inverters with LCL-filter considering the GVFR. The stability of the current loop without GVFR is firstly investigated through the poles distribution analysis, the critical frequency and stability boundary have been identified. Then, the study extends the analysis to the stability considering the GVFR. It has been revealed that, in a weak power system, the GVFR will significantly alter the system stability. Based on the stability analysis in different frequency ranges, this paper recommends a robust design for LCL-filter in the grid-connected application. Through theoretical and experimental verification, the parameters designed inside the robust area are more robust to the variation of grid inductance.

Then, *Chapter 3* deals with the graphical illustration of several compensation schemes for the intrinsic time delays in the digital micro-processor. A unified explanation and evaluation method is presented to compare various delays compensation schemes, using which the essential reason of these compensation schemes is clearly revealed. Moreover, based on the evaluation, this thesis has proposed an improved compensation method, with which the compensation performance is enhanced compared to existing methods. Furthermore, the proposed

method is tested in a LCL-filtered inverter platform for verifying the delay compensation effectiveness.

Chapter 4 investigates the stability of power-electronics based power system, where multiple grid-connected inverters are installed to the same point. A grid current dividing model, consisting of interactive current and common current, is presented in this thesis. Through this dividing model, the stability of paralleled system can be analyzed through the stability of two currents. The resonant phenomenon that interactive resonant current circulates between two paralleled inverters is first revealed in this thesis [20]. Two stability regions are then identified using the root loci plot and analysis in the *z*-domain. Simulation and experimental results verify all the analysis in the paper.

5.2. MAIN CONTRIBUTIONS

The main contributions and significance throughout this the whole thesis are listed as follows (from the author's point of view):

- ***Robust Design Guideline of LCL-Filter and New Identified Resonance Frequency Boundaries for Grid-Connected Inverters Considering Grid Voltage Feedforward Regulator***

Through stability analysis of grid-connected inverter with GVFR, different resonance frequencies have been identified under the weak grid condition. Different from the situation with single current loop, the additional GVFR will significantly alter system stability. A design guideline of LCL-filter for more robustness against the grid impedance variation is also given.

- ***Comprehensive Evaluation and Comparison of Different Delay Compensation Methods***

A comprehensive evaluation and comparison of existing digital delays compensation methods, which are independent of system modeling information and accuracy, have been presented. Besides, the essential reasoning for these compensation methods is also given.

- ***Proposed Delay Compensation Scheme with Improved Performance***

The same geometrical reasoning is used to devise an improved delay compensation filter, whose final structure is very similar to that of the first order filter based method, but offers a better phase delay compensation capability.

- ***Proposed Current Separating Model for Multi-Parallel Grid-Connected Inverters***

A proposed current separating model has been adopted for analyzing the stability of multi-parallel grid inverters with LCL-filters. Using this model, it has been revealed that two current components have different stability ranges. The whole stability of parallel system can be divided into the stability analysis of two different current components.

5.3. FUTURE PERSPECTIVES

- **Control system with other control structure**

All the analysis in this thesis adopts the basic linear control structure, such as PI or PR controller. In fact, some control structures, like hysteresis control or other advanced control structures, are also applied in the grid-connected system.

- **Stability analysis of the control system taking account of outer loops**

Apart from the inner current loop, the outer loops (such as DC-link voltage control loop and PLL) also have significant impacts on the response and system stability. Modeling and analysis of the control system considering the outer loops is also worth to investigate.

- **Non-linear behavior of components**

All the stability analysis in this thesis is based on the assumption that the non-linear behavior of inductor and capacitor are neglected. However, the non-linear behavior may change the values of inductance or capacitance, making the system modeling not accurate. Therefore, the non-linear behavior should be considered in the future analysis.

- **Paralleled inverters with different power rating**

An main assumption in this thesis is that all the inverters in the renewable energy generation system are identical. However, it is normal that in a paralleled system, the inverters are different from each other. The parallel operation with different power rating is difficult to analyze and still needs more investigation in the future.

- **Control scheme and filter design considering the grid impedance variation**

The robustness of the grid-connected inverters against the grid impedance variation is also an important issue. Because the modern power system tends to be weak when a high penetration of renewables is installed, the robust design of control scheme is also interesting.

LITERATURE LIST

[1] F. Blaabjerg, Y. Yang, K. Ma and X. Wang, "Power electronics-the key technology for renewable energy system integration," in *Proc. of the 4th International Conference on Renewable Energy Research and Applications (ICRERA)*, Nov. 2015, pp. 1618-1626.

[2] The official website of Denmark, "A world-leader in wind energy," [Online]. Available: http://denmark.dk/en/green-living/wind-energy/.

[3] Global Wind Energy Council, "Global Wind Report 2016," [Online]. Available: http://www.gwec.net/global-figures/global-offshore/.

[4] International Energy Agency, "Snapshot of Global Photovoltaic Markets 2017," [Online]. Available: www.iea-pvps.org.

[5] F. Blaabjerg, R. Teodorescu, M. Liserre, and A. V. Timbus, "Overview of control and grid synchronization for distributed power generation systems," *IEEE Trans. Ind. Electron*., vol. 53, no. 5, pp. 1398–1409, Oct. 2006.

[6] X. Wang, F. Blaabjerg, and W. Wu, "Modeling and analysis of harmonic stability in an AC power-electronics-based power system," *IEEE Trans. Power Electron*., vol. 29, no. 12, pp. 6421–6432, Dec. 2014.

[7] J.H.R. Enslin, P.J.M. Heskes, "Harmonic interaction between a large number of distributed power inverters and the distribution network," *IEEE Trans. Power Electron*., vol. 19, no. 6, pp. 1586-1593, Nov. 2004.

[8] J. Agorreta, M. Borrega, J. Lopez, and L. Marroyo, "Modeling and control of N-paralleled grid-connected inverters with LCL filters coupled due to grid impedance in PV plants," *IEEE Trans. Power Electron*., vol. 26, no. 3, pp. 770-1194, Mar. 2011.

[9] A. Badram, A. Davoudi, and R. S. Balog, "Control and circuit techniques to mitigate partial shading effects in photovoltaic arrays," *IEEE J. Photovoltaics*, vol. 2, no. 4, pp. 532–546, Oct. 2012.

[10] J. He, Y. Li, D. Bosnjak, "Investigation and Active Damping of Multiple Resonances in a Parallel-Inverter-Based Microgrid," *IEEE Trans. Power Electron.*, vol. 28, no. 1, pp. 234-246, Jan. 2013.

[11] X. Wang, F. Blaabjerg, M. Liserre, Z. Chen, J. He, and Y. W. Li, "An active damper for stabilizing power-electronics-based AC systems," *IEEE Trans. Power Electron*., vol. 29, no. 7, pp. 3318–3329, Jul. 2014.

[12] M. Lu, X. Wang, P.C. Loh, F. Blaabjerg, "Interaction and Aggregated Modeling of Multiple Paralleled Inverters with LCL Filter," in *Proc. of 2015 IEEE Energy Conversion Congress and Exposition* (*IEEE ECCE 2015*), Montreal, CA, Sep. 2015, pp. 1-7.

[13] M. Lu, F. Blaabjerg, X. Wang, "Interaction admittance based modeling of multi-paralleled grid-connected inverter with LCL-filter," in *Proc. of 2016 IEEE 2nd Annual Southern Power Electronics Conference* (*IEEE SPEC 2016*), Auckland, NZ, Dec. 2016, pp. 1-7.

[14] C. Yoon, H. Bai, R. Beres, X. Wang, F. Blaabjerg, "Harmonic stability assessment for multi-paralleled, grid-connected inverters," *IEEE Trans. Sustain. Energy*., vol. 18, no. 3, pp. 888--895, May 2016.
[15] B.K. Bose and H.A. Sutherland, "A high performance pulse-width modulator for an inverter-fed drive system using a microcomputer," *IEEE Trans. Ind. Appl*., vol. 19, pp. 235-243. Mar./Apr. 1983.
[16] *Standard for Interconnecting Distributed Resources with Electric Power Systems*, IEEE Standard 1547-2003, 2003.
[17] Y. Tang, P.C. Loh, P. Wang, F.H. Choo, and F. Gao, "Exploring inherent damping characteristic of LCL-filters for three-phase grid-connected voltage source inverters," *IEEE Trans. Power Electron*., vol. 27, no. 3, pp. 1433–1443, Mar. 2012.
[18] E. Twining and D. G. Holmes, "Grid current regulation of a three-phase voltage source inverter with an *LCL* input filter," *IEEE Trans. Power Electron*., vol. 18, no. 3, pp. 888–895, May 2003.
[19] M. Liserre, F. Blaabjerg, and S. Hansen, "Design and control of an LCL filter-based three-phase active rectifier," *IEEE Trans. Ind. Appl*., vol. 41, no. 5, pp. 1281–1291, Sep./Oct. 2005.
[20] M. Lu; X. Wang; P.C. Loh; F. Blaabjerg, "Resonance Interaction of Multi-Parallel Grid-Connected Inverters with LCL Filter," *IEEE Trans. on Power Electron*. , vol. 32, no. 2, pp. 894–899, Feb. 2017.
[21] S. Chung, "A phase tracking system for three phase utility interface inverters," *IEEE Trans. Power Electron*., vol. 15, no. 3, pp. 431–438, May 2000.
[22] Y. Huang et al., "Modeling of VSC connected to weak grid for stability analysis of DC-link voltage control," *IEEE J. Emerg. Select. Topics Power Electron*., vol. 3, no. 4, pp. 1193–1204, Dec. 2015.
[23] Y. Huang, X. Yuan, J. Hu, P. Zhou, and D. Wang, "DC-bus voltage control stability affected by AC-bus voltage control in VSCs connected to weak AC grids," *IEEE J. Emerg. Select. Topics Power Electron*., vol. 4, no. 2, pp. 445–458, Jun. 2016.
[24] Z. Xin, X. Wang, P.C. Loh, F. Blaabjerg, "Grid-current feedback control for LCL-filtered grid converters with enhanced stability," *IEEE Trans. Power Electron*., vol. 32, no. 4, pp. 3216-3228, Apr. 2017.
[25] J. Yin, S. Duan, B. Liu, "Stability analysis of grid-connected inverter with *LCL* filter adopting a digital single-loop controller with inherent damping characteristic," *IEEE Trans. Ind. Inf.*, vol. 9, no. 2, pp. 1104-1112, May. 2013.
[26] H. Zhou, Y. Li, N.R. Zargari, "Selective harmonic compensation (SHC) PWM for grid-interfacing high-power converters," *IEEE Trans. Power Electron*., vol. 29, no. 3, pp. 1118–1127, Mar. 2014.
[27] M. Xue, Y. Zhang, Y. Kang, Y. Yi, S. Li, and F. Liu, "Full feedforward of grid voltage for discrete state feedback controlled grid-connected inverter with *LCL* filter," *IEEE Trans. Power Electron*., vol. 27, no. 10, pp. 4234– 4247, Oct. 2012.

[28] T. Abeyasekera, C. M. Johnson, D. J. Atkinson, and M. Armstrong, "Suppression of line voltage related distortion in current controlled grid connected inverters," *IEEE Trans. Power Electron*., vol. 20, no. 6, pp. 1393–1401, Nov. 2005.

[29] X. Wang, X. Ruan, S. Liu, and C. K. Tse, "Full Feedforward of Grid Voltage for Grid-Connected Inverter With LCL Filter to Suppress Current Distortion Due to Grid Voltage Harmonics," *IEEE Trans. Power Electron.*, vol. 25, pp. 3119-3127, 2010.

[30] Y. Zhang, M. Xue, M. Li, and Y. Kang, "Co-design of the *LCL* filter and control for grid-connected inverters," *Journal of Power Electronics*, vol. 14, no. 5, pp. 1047-1056, Sep. 2014.

[31] C. Zou, B. Liu, S. Duan, and R. Li, "A feedforward scheme to improve system stability in grid-connected inverter with *LCL* filter," in *Proc. IEEE Energy Convers. Congr. Expo*., 2013, pp. 4476–4480.

[32] J. Wang, Y. Song, A. Monti, "A study of feedforward control on stability of grid-parallel inverter with various grid impedance," in *Proc. IEEE 5th International Symposium on Power Electronics for Distributed Generation Systems (PEDG)*, pp. 1-8, June 2014.

[33] B. S. Buso and P. Mattavelli, "Digital control in power electronics," in *Synthesis Lectures on Power Electronics*. San Rafael, CA: *Morgan & Claypool,* 2006.

[34] D. G. Holmes, T. A. Lipo, B. P. McGrath, and W. Y. Kong, "Optimized design of stationary frame three phase AC current regulators," *IEEE Trans. Ind. Inf*., vol. 24, no. 11, pp. 2417-2426, Nov. 2009.

[35] F. Blaabjerg, Z. Chen, S.B. Kjaer, "Power electronics as efficient interface in dispersed power generation systems," *IEEE Trans. Power Electron*., vol. 19, no. 5, pp. 1184-1194, Sept. 2004.

[36] L. Kocewiak, "Harmonics in large offshore wind farms," Ph.D. dissertation, Aalborg Univ., Aalborg, Denmark, 2012.

[37] R. Teodorescu, F. Blaabjerg, M. Liserre, et al, "Proportional-resonant controllers and filters for grid-connected voltage-source converters," *IEE Proceedings Electron. Power Appl.,* 2006,153 (5): 750-762.

[38] C. Zou, B. Liu, S. Duan, and R. Li, "Influence of delay on system stability and delay optimization of grid-connected inverters with LCL filter," *IEEE Trans. Ind. Inf*., vol. 10, no. 3, pp. 1775–1784, Aug. 2014.

[39] M. Lu, X. Wang, F. Blaabjerg, S.M. Muyeen, "Grid-voltage-feedforward active damping for grid-connected inverter with LCL filter," in *Proc. IEEE APEC, 2016*, vol. 1, pp. 1941–1946.

[40] R. Teodorescu, F. Blaabjerg, U. Borup, and M. Liserre, "A new control structure for grid-connected LCL PV inverters with zero steady-state error and selective harmonic compensation," in *Proc. IEEE APEC, 2004*, vol. 1, pp. 580–586.

[41] J. Wang, J. D. Yan, L. Jiang, and J. Zou, "Delay-dependent stability of single-loop controlled grid-connected inverters with LCL filters," *IEEE Trans. Power Electron*., vol. 31, no. 1, pp. 743–757, Jan. 2016.

[42] Z. Xin, P. C. Loh, X. Wang, F. Blaabjerg, and Y. Tang, "Highly Accurate Derivatives for LCL-Filtered Grid Converter with Capacitor Voltage Active Damping," *IEEE Trans. Power Electron*., vol. 31, no.5, pp. 3612-3625, May. 2016.

[43] Q. Yan, X. Wu, X. Yuan, and Y. Geng, "An improved grid-voltage feedforward strategy for high-power three-phase grid-connected inverters based on the simplified repetitive predictor," *IEEE Trans. Power Electron*., vol. 31, no. 5, pp. 3880–3897, May 2016.

[44] S. Bibian and H. Jin, "Time delay compensation of digital control for DC switchmode power supplies using prediction techniques," *IEEE Trans. Power Electron*., vol. 15, no. 5, pp. 835–842, Sep. 2000.

[45] P. Mattavelli, F. Polo, F. Dal Lago, and S. Saggini, "Analysis of control delay reduction for the improvement of UPS voltage-loop bandwidth," *IEEE Trans. Ind. Electron*., vol. 55, no. 8, pp. 2903–2911, Aug. 2008.

[46] M. Lu, X. Wang, P.C. Loh, F. Blaabjerg, T. Dragicevic, "Graphical Evaluation of Time-Delay Compensation Techniques for Digitally Controlled Converters," *IEEE Trans. on Power Electron*., *Early access*, Mar. 2017.

[47] C. Chen, J. Xiong, Z. Wan, J. Lei, and K. Zhang, "A Time delay compensation method based on area equivalence for active damping of an LCL-type converter," *IEEE Trans. Power Electron*., vol. 32, no. 1, pp. 762-772, January 2017.

[48] C. Citro, P. Siano, C. Cecati, "Designing inverters' current controllers with resonance frequencies cancellation," *IEEE Trans. Ind. Electron*., vol. 63, no. 5, pp. 3072–3080, May. 2016.

[49] X. Li, X. Wu, Y. Geng, X. Yuan, C. Xia, and X. Zhang, "Wide damping region for LCL-type grid-connected inverter with an improved capacitor current-feedback method," *IEEE Trans. Power Electron*., vol. 30, no. 9, pp. 5247–5259, Sep. 2015.

[50] D. Pan, X. Ruan, C. Bao, W. Li, X. Wang, "Capacitor-Current-Feedback active damping with reduced computation delay for improving robustness of LCL-type grid-connected inverter," *IEEE Trans. Power Electron*., vol. 29, no. 7, pp. 3414-3426, July. 2014.

[51] L. Harnefors, A. G. Yepes, A. Vidal, and J. Doval-Gandoy, "Passivity based stabilization of resonant current controllers with consideration of time delay," *IEEE Trans. Power Electron*., vol. 29, no. 12, pp. 6260–6263, Dec. 2014.

[52] V. Miskovic, V. Blasko, T. Jahns, A. Smith, and C. Romenesko, "Observer based active damping of LCL resonance in grid connected voltage source converters," *IEEE Trans. Ind. Appl*., vol. 50, no. 6, pp. 3977–3985, Nov./Dec. 2014.

[53] S. Bibian and H. Jin, "High Performance Predictive Dead-Beat Digital Controller for DC Power Supplies," *IEEE Trans. Power Electron*., vol. 17, no. 3, pp. 420–427, May. 2002.

[54] A. Kawamura, T. Haneyoshi, and R. G. Hoft, "Deadbeat controlled PWM inverter with parameter estimation using only voltage sensor," in *Proc. Power Electronics Specialists Conf.*, Apr. 1986, pp. 118–125.

[55] T. Nussbaumer, M. L. Heldwein, G. Gong, S. D. Round, and J. W. Kolar, "Comparison of prediction techniques to compensate time delays caused by digital control of a three-phase buck-type PWM rectifier system," *IEEE Trans. Ind. Electron*., vol. 55, no. 2, pp. 791–799, Feb. 2008.

[56] X. Ruan, X. Wang, D. Pan, D. Yang, W. Li, C. Bao, Control Techniques for LCL-Type Grid-Connected Inverters. Beijing, China: *Science Press*, 2015, pp. 72-93.

[57] R. Juntunen, J. Korhonen, T. Musikka, L. Smirnova, O. Pyrhönen, and P. Silventoinen, "Identification of resonances in parallel connected grid Inverters with LC- and LCL-filters," in *Proc. of the IEEE Applied Power Electronics Conference and Exposition (APEC)*, 2015, pp. 2122-2127.

[58] M. Lu, X. Wang, P.C. Loh, F. Blaabjerg, "An analysis method for harmonic resonance and stability of multi-paralleled *LCL*-filtered inverters," in *Proc. IEEE 6th International Symposium on Power Electronics for Distributed Generation Systems (PEDG 2015)*, Aachen, Germany, pp. 1-6.

[59] P. Dang, T. Ellinger and J. Petzoldt, "Dynamic interaction analysis of APF systems," *IEEE Transactions on Industrial Electronics*, vol. 26, no. 9, pp. 4467- 4473, Sep. 2014.

[60] S. Skogestad and I. Postlethwaite, *Multivariable Feedback Control: Analysis and Design*. New York: Wiley, 1997.

[61] C. Yu, X. Zhang, F. Liu, and F. Li, "Modeling and Resonance Analysis of Multi-parallel Inverters System under Asynchronous Carriers Conditions," *IEEE Trans. Power Electron.*., vol. 32, no. 4, pp. 3192–3205, Apr. 2017.

[62] F. Cavazzana, P. Mattavelli, M. Corradin, and I. Toigo, "Grid sensitivity considerations on multiple parallel inverters systems," in in *Proc. of 2016 IEEE 8th International Power Electronics and Motion Control Conference (IPEMC-ECCE Asia)*, May 2016, pp. 993–999.

[63] S. Banerjee and G. C. Verghese, *Nonlinear Phenomena in Power Electronics: Attractors, Bifurcations, Chaos and Nonlinear Control*. Piscataway, NJ: IEEE Press, 2001.

[64] D. G. Holmes and T. A. Lipo, Pulse Width Modulation for Power Converters. New York: *IEEE Press*, 2003.

[65] S.G. Parker, B. P. McGrath, D.G. Holmes, "Regions of Active Damping Control for LCL Filters," *IEEE Trans. Ind. Appl*., vol. 50, no. 1, pp. 424-432, Jan./Feb. 2014.

[66] L. Harnefors, A. G. Yepes, A. Vidal, and J. Doval-Gandoy, "Passivitybased controller design of grid-connected VSCs for prevention of electrical resonance instability," *IEEE Trans. Ind. Electron*., vol. 62, no. 2, pp. 702– 710, Feb. 2015.

[67] K. Warwick and D. Rees, Industrial Digital Control Systems (*IEE Control Engineering Series 37*). Stevenage, U.K: *Pereginus*, 1988.

[68] A. Kuperman, "Proportional-resonant current controllers design based on desired transient performance," *IEEE Trans. Power Electron*., vol. 30, no. 10, pp. 5341–5345, Oct. 2015.

[69] M. Liserre, R. Teodorescu, and F. Blaabjerg, "Stability of photovoltaic and wind turbine grid-connected inverters for a large set of grid impedance values," *IEEE Trans. Power Electron*., vol. 21, no. 1, pp. 263–272, Jan. 2006.

[70] E. I. Jury, *Theory and Application of the Z-Transform Method*. New York: Wiley, 1964.

[71] A. Reznik, M. Simoes, A. Al-Durra, and S. Muyeen, "LCL filter design and performance analysis for grid-interconnected systems," *IEEE Trans. Ind. Appl*., vol. 50, no. 2, pp. 1225–1232, Mar. 2014.

[72] Q. Liu, L. Peng, Y. Kang, "A Novel Design and Optimization Method of an LCL filter for a shunt Active Power Filter," *IEEE Trans. Ind. Electron*., vol. 61, no. 8, pp. 4000-4010, Aug. 2014.

[73] T. Itkonen, J. Luukko, A. Sankala, and T. Laakkonen,"Modeling and analysis of the dead-time effects in parallel PWM two-level three-phase voltage-source inverters," *IEEE Trans. Power Electron*., vol. 24, no. 11, pp. 2446–2455, Nov. 2009.

[74] Wikipedia, "Jury stability criterion," [Online]. Available: https://en.wikipedia.org/wiki/Jury_stability_criterion.

[75] M. B. Sa¨ıd-Romdhane, M. W. Naouar, I. S. Belkhodja, and E. Monmasson, "Simple and systematic LCL filter design for three-phase grid-connected power converters," *Math. Comput. Simul*., vol. 130, pp. 181–193, 2016.